FINAL REPORT
NASA Grant 3684
Lava Flow Dynamics

This grant originally had four major tasks, all of which were addressed to varying extents during the course of the research:

- Measure the fractal dimensions of lava flows as a function of topography, substrate, and rheology.
- The nature of lava tube systems and their relation to flow fields.
- A quantitative assessment of lava flow dynamics in light of the fractal nature of lava flow margins.
- Development and application of a new remote sensing tool based on fractal properties.

During the course of the research, the project expanded to include the projects listed below. This work was also funded in part by the National Science Foundation through a graduate fellowship to Rachel Friedman.

- A comparison of what we can learn from remote sensing studies of lava flow morphology and from studies of samples of lava flows.
- Study of a terrestrial analog of the nakhlites, one of the groups of meteorites from Mars.
- Study of the textures of Hawaiian basalts as an aid in understanding the dynamics (flow rates, inflation rates, thermal history) of flow interiors.

In addition, during the first year an educational task was included. This entailed development and writing of a teacher's guide and activity set to accompany the lunar sample disk when it is sent to schools. This resulted in publication of **EP-306**, referenced below.

Publications

Publications in refereed journals

Bruno, B. C., Taylor, G. J., Rowland, S. K. and Baloga, S.M. (1994) Quantifying the effect of rheology on lava-flow margins using fractal geometry. *Bull. Volc.*, **56**, 193-206.

Bruno, B. C. and Taylor, G. J. (1995) Morphologic identification of Venusian lavas. *Geophys. Res. Lett.* **22**, 1897-1900.

Bruno, B. C., Baloga, S. M., and Taylor, G. J. (1996) Modeling gravity-driven flows on an inclined plane. *J. Geophys. Res* **101**, 11,565-11,577.

Educational publication

Taylor, G.J., Martel, L.V. and Bays, B. (1994) *Exploring the Moon: A Teacher's Guide with Activities*, **NASA EP-306**, 148 p.

Abstracts and extended abstracts

Taylor, G. J. (1992) Fractal properties of lava tube systems. *EOS* **73**, 648.

Bruno, B. C. and Taylor, G. J. (1992) Effect of rheology on plan-view shapes of lava flows. *EOS* **73**, 648.

Bruno, B. C., Taylor, G. J., and Lopes-Gautier, R. M. C. (1993) Quantifying the effect of rheology on plan-view shapes of lava flows. *Lunar and Planetary Science XXIV*, 207-208.

Lopes-Gautier, R., Bruno, B. C., Taylor, G. J., and Kilburn, C. R. J. (1993) Martian lavas: three complementary remote sensing techniques to derive flow properties. . *Lunar and Planetary Science XXIV,* 899-900.

Bruno, B. C., Taylor, G. J., Rowland, S. K., and Baloga, S. M. (1993) Flow margins: indicators of underlying fluid dynamics processes? *IAVCEI Abstracts*, 13.

Taylor, G. J. and Bruno, B. C. (1993) Fractal properties of lava flows: Clues to eruption rates, emplacement mechanisms, and rheology. *Geol. Soc. Amer. Annual Meeting*, A-343.

Bruno, B. C., Baloga, S. M., Taylor, G. J., and Tatsumura, M. J. (1994) Lava flow rheology: A comparison of data and theory. *Lunar and Planetary Science XXV*, 189-190.

Taylor, G. J., Bruno, B. C., and Self, S. (1994) Slow emplacement of flood basalts: evidence from fractal properties of lava flows. *Lunar and Planetary Science XXV*, 1383-1384.

Friedman, R. C., McCoy, T. J., and Taylor, G. J. (1994) Constraints on the physical details of nakhlite formation. *Lunar and Planetary Science XXV*, 391-392.

Bruno, B. C. and Taylor, G. J. (1995) Morphologic identification of venusian lavas: implications for emplacement of long lava flows. *Lunar and Planetary Science XXVI*, 185-186.

Coombs, C. R., Taylor, G. J., and Rowland, S. K. (1995) The formation and evolution of lava tubes. *Lunar and Planetary Science XXVI*, 279-280.

Friedman, R. C., Taylor, G. J., and Treiman, A. H. (1995) Processes in thick lava flows: nakhlites (Mars) and Theo's flow (Ontario, Earth). *Lunar and Planetary Science XXVI*, 429-430.

Lopes-Gautier, R., Bruno, B. C., Taylor, G. J., and Kilburn, C. (1995) Lava flows on Alba Patera: analysis of flow properties using three complementary models. *Lunar and Planetary Science XXVI*, 861-862.

Lopes-Gautier, R., Bruno, B. C., Taylor, G. J., Smythe, W., and Kilburn, C. (1996) Analysis of Martian lava flows using three complementary models. *Lunar and Planetary Science XXVII*, 771-772.

Future publications

NASA Grant 3684 will be acknowledged in future publications now in preparation. These will deal with Theo's flow (the martian meteorite analog), Hawaiian basalts, lava tube formation, and computer modeling of lava flows with explicit attention paid to the shapes of the margins. Although other support contributed to these studies, NASA support was essential.

Inventions

No inventions were created during the course of this work.

REPORT OF INVENTIONS AND SUBCONTRACTS

(Pursuant to "Patent Rights" Contract Clause) (See Instructions on Reverse Side.)

Form Approved
OMB No. 0704-0297
Expires Jun 30, 1992

1a. NAME OF CONTRACTOR / SUBCONTRACTOR	c. CONTRACT NUMBER	2a. NAME OF GOVERNMENT PRIME CONTRACTOR	c. CONTRACT NUMBER	3. TYPE OF REPORT (X one)
G. Jeffrey Taylor	NASA Grant 3684	Univ. of Hawaii		a. INTERIM ☐ b. FINAL ☐
b. ADDRESS (Include ZIP Code)	d. AWARD DATE (YYMMDD)	b. ADDRESS (Include ZIP Code)	d. AWARD DATE (YYMMDD)	4. REPORTING PERIOD (YYMMDD)
2525 Correa Rd., Honolulu, HI 96822	3/1/93	Honolulu, HI 96822		a. FROM b. TO

SECTION I – SUBJECT INVENTIONS

5. "SUBJECT INVENTIONS" REQUIRED TO BE REPORTED BY CONTRACTOR / SUBCONTRACTOR (If "None," so state)

a. NAME(S) OF INVENTOR(S) (Last, First, MI)	b. TITLE OF INVENTION(S)	c. DISCLOSURE NO., PATENT APPLICATION SERIAL NO. OR PATENT NO.	d. ELECTION TO FILE PATENT APPLICATIONS				e. CONFIRMATORY INSTRUMENT OR ASSIGNMENT FORWARDED T CONTRACTING OFFICER	
			(1) United States		(2) Foreign			
			(a) Yes	(b) No	(a) Yes	(b) No	(1) Yes	(2) No
NO NO	NONE							

f. EMPLOYER OF INVENTOR(S) NOT EMPLOYED BY CONTRACTOR / SUBCONTRACTOR		g. ELECTED FOREIGN COUNTRIES IN WHICH A PATENT APPLICATION WILL BE FILED	
(1) (a) Name of Inventor (Last, First, MI)	(2) (a) Name of Inventor (Last, First, MI)	(1) Title of Invention	(2) Foreign Countries of Patent Application
(b) Name of Employer	(b) Name of Employer		
(c) Address of Employer (Include ZIP Code)	(c) Address of Employer (Include ZIP Code)		

SECTION II – SUBCONTRACTS (Containing a "Patent Rights" clause)

6. SUBCONTRACTS AWARDED BY CONTRACTOR / SUBCONTRACTOR (If "None," so state)

a. NAME OF SUBCONTRACTOR(S)	b. ADDRESS (Include ZIP Code)	c. SUBCONTRACT NO.(S)	d. DFAR "PATENT RIGHTS"		e. DESCRIPTION OF WORK TO BE PERFORMED UNDER SUBCONTRACT(S)	f. SUBCONTRACT DATES (YYMMDD)	
			(1) Clause Number	(2) Date (YYMM)		(1) Award	(2) Estimated Completion
NONE	NONE						

SECTION III – CERTIFICATION

7. CERTIFICATION OF REPORT BY CONTRACTOR / SUBCONTRACTOR (Not required if ☐ Small Business or ☐ Non-Profit organization.) (X appropriate box)

a. NAME OF AUTHORIZED CONTRACTOR / SUBCONTRACTOR OFFICIAL (Last, First, MI)	c. I certify that the reporting party has procedures for prompt identification and timely disclosure of "Subject Inventions," that such procedures have been followed and that all "Subject Inventions" have been reported.	
G. Jeffrey Taylor		
b. TITLE	d. SIGNATURE	e. DATE SIGNED
Professor / P.I.	[signature]	8/11/97

DD Form 882, OCT 89

Previous editions are obsolete.

971/284

DD FORM 882 INSTRUCTIONS

GENERAL

This form is for use in submitting INTERIM and FINAL invention reports to the Contracting Officer and for use in the prompt notification of the award of subcontracts containing a "Patent Rights" clause. If the form does not afford sufficient space, multiple forms may be used or plain sheets of paper with proper identification of information by Item Number may be attached.

An INTERIM report is due at least every 12 months from the date of contract award and shall include (a) a listing of "Subject Inventions" during the reporting period, (b) a certification of compliance with required invention identification and disclosure procedures together with a certification of reporting of all "Subject Inventions," and (c) any required information not previously reported on subcontracts awarded during the reporting period and containing a "Patent Rights" clause.

A FINAL report is due within 6 months if contractor is a small business firm or domestic nonprofit organization and within 3 months for all others after completion of the contract work and shall include (a) a listing of all "Subject Inventions" required by the contract to be reported, and (b) any required information not previously reported on subcontracts awarded during the course of or under the contract and containing a "Patent Rights" clause.

While the form may be used for simultaneously reporting inventions and subcontracts, it may also be used for reporting, promptly after award, subcontracts containing a "Patent Rights" clause.

Dates shall be entered where indicated in certain Items on this form and shall be entered in four or six digit numbers in the order of year and month (YYMM) or year, month and day (YYMMDD). Example: April 1986 should be entered as 8604 and April 15, 1986 should be entered as 860415.

Item 1a. Self-explanatory.

Item 1b. Self-explanatory.

Item 1c. If "same" as item 2c, so state.

Item 1d. Self-explanatory.

Item 2a. If "same" as item 1a, so state.

Item 2b. Self-explanatory.

Item 2c. Procurement Instrument Identification (PII) number of contract (DFAR 4.7003).

Item 2d thru 5e. Self-explanatory.

Item 5f. The name and address of the employer of each inventor not employed by the contractor or subcontractor is needed because the Government's rights in a reported invention may not be determined solely by the terms of the "Patent Rights" clause in the contract.

Example 1: If an invention is made by a Government employee assigned to work with a contractor, the Government rights in such an invention will be determined under Executive Order 10096.

Example 2: If an invention is made under a contract by joint inventors and one of the inventors is a Government employee, the Government's rights in such an inventor's interest in the invention will also be determined under Executive Order 10096, except where the contractor is a small business or nonprofit organization, in which case the provisions of Section 202 (e) of P.L. 96-517 will apply.

Item 5g (1). Self-explanatory.

Item 5g (2). Self-explanatory with the exception that the contractor or subcontractor shall indicate, if known at the time of this report, whether applications will be filed under either the Patent Cooperation Treaty (PCT) or the European Patent Convention (EPC). If such is known, the letters PCT or EPC shall be entered after each listed country.

Item 6a. Self-explanatory.

Item 6b. Self-explanatory.

Item 6c. Self-explanatory.

Item 6d. Patents Rights Clauses are located in FAR 52.227.

Item 6e thru 7b. Self-explanatory.

Item 7c. Certification not required by small business firms and domestic nonprofit organizations.

Bull Volcanol (1994) 56:193–206

HIGP Contribution No. 764

Bulletin of
Volcanology

Quantifying the effect of rheology on lava-flow margins using fractal geometry

B. C. Bruno[1], **G. J. Taylor**[1], **S. K. Rowland**[1], **S. M. Baloga**[2]*

[1] Hawaii Institute of Geophysics and Planetology, University of Hawaii at Manoa, 2525 Correa Road, Honolulu, Hawaii 96822, USA
[2] Jet Propulsion Laboratory, NASA, California Institute of Technology, 4800 Oak Grove Drive, Pasadena, California 91109, USA

Received: June 6, 1993/Accepted: March 18, 1994

Abstract. This study aims at quantifying the effect of rheology on plan-view shapes of lava flows using fractal geometry. Plan-view shapes of lava flows are important because they reflect the processes governing flow emplacement and may provide insight into lava-flow rheology and dynamics. In our earlier investigation (Bruno et al. 1992), we reported that flow margins of basalts are fractal, having a characteristic shape regardless of scale. We also found we could use fractal dimension (D, a parameter which quantifies flow-margin convolution) to distinguish between the two endmember types of basalts: a'a (D: 1.05–1.09) and pahoehoe (D: 1.13–1.23). In this work, we confirm those earlier results for basalts based on a larger database and over a wider range of scale (0.125 m–2.4 km). Additionally, we analyze ten silicic flows (SiO_2: 52–74%) over a similar scale range (10 m–4.5 km). We note that silicic flows tend to exhibit scale-dependent, or non-fractal, behavior. We attribute this breakdown of fractal behavior at increased silica contents to the suppression of small-scale features in the flow margin, due to the higher viscosities and yield strengths of silicic flows. These results suggest we can use the fractal properties of flow margins as a remote-sensing tool to distinguish flow types. Our evaluation of the nonlinear aspects of flow dynamics indicates a tendency toward fractal behavior for basaltic lavas whose flow is controlled by internal fluid dynamic processes. For silicic flows, or basaltic flows whose flow is controlled by steep slopes, our evaluation indicates non-fractal behavior, consistent with our observations.

Key words: fractals – lava – rheology – remote sensing

* *Present address:* Proxemy Research Inc., 20528 Farcroft Lane, Laytonsville, Maryland 20882, USA

Correspondence to: B. C. Bruno

Introduction

Plan-view shapes of lava flows reflect the processes governing flow emplacement; they are frozen snapshots of the final moments of flow. As such, they provide insight into the final stages of lava-flow dynamics and rheological state. Plan-view shapes and other morphological characteristics have been studied extensively and important quantitative parameters have been developed to extract rheological properties and eruption and emplacement processes of lava flows. Useful parameters include flow length and width as indicators of eruption rate and duration (Walker 1973; Hulme and Fielder 1977); widths and thicknesses of flows to estimate yield strengths (Hulme 1974); widths of distal lobes to deduce rheological properties and SiO_2 content (Wadge and Lopes 1991); channel depth and width and surface speed to estimate viscosity (Shaw et al. 1968); total area and volume to estimate maximum flow rates and minimum emplacement times (Shaw and Swanson 1970); flow length and width coupled with levee and channel width to yield effusion rate (Crisp and Baloga 1990); average thickness and the ratio of maximum width to maximum length to calculate eruption duration (Lopes and Kilburn 1990); and ridge heights and spacings to estimate viscosity of flow interiors (Fink and Fletcher 1978; Fink 1980). Use of these measurements has led to improved insight into lava-flow dynamics and planetary volcanism, but many questions about their quantitative use remain.

We have been using a new approach to quantitatively characterize lava-flow morphology: the fractal properties of flow margins. In our preliminary report (Bruno et al. 1992), we showed that the perimeters of basaltic flows are fractal, and have characteristic fractal dimensions. Fractals are objects (real or mathematical) that look the same at all scales (Mandelbrot 1967, 1983). Many geologic features exhibit such 'self-similar' behavior (e.g. rocky coastlines, topography, river networks). A qualitative example of self-similar behavior of a lava-flow margin appears in Fig. 1. We believe that measurement of fractal properties of lava flows

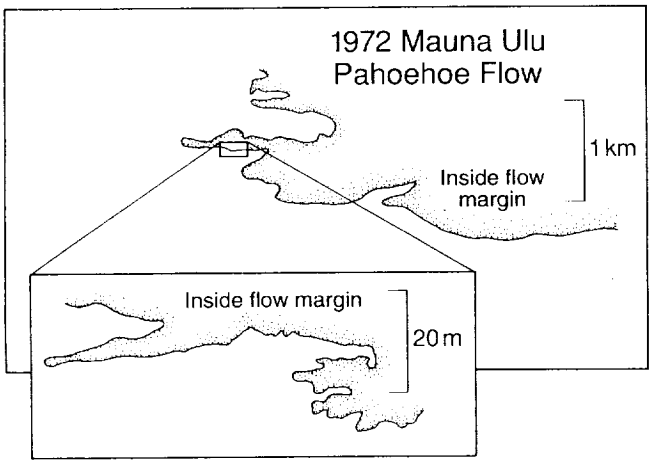

Fig. 1. Margin of a typical pahoehoe flow from the 1972 eruption of Mauna Ulu, Kilauea volcano with small section enlarged to show self-similarity. The similar shapes of the entire flow margin and the enlarged section at different scales suggests fractal behavior

Fig. 2 Fractal dimensions (D) of selected curves: **a** $D=1.00$; **b** $D=1.01$; **c** $D=1.10$. The complex curves (b, c) are longer and are more plane-filling than (a) and thus have $D>1$. Since these curves are contained in a plane ($D=2$), they have D between 1 and 2 (following Garcia 1991)

will shed light on flow dynamics, eruption rates, and rheology, and will prove to be a useful method for quantifying the morphology of lava flows in inaccessible areas of the Earth as well as on other planets by means of remote sensing.

The key parameter we derive is fractal dimension. Fractal dimension (D) is based on a similar concept as topological dimension (D_T). For example, a line can be contained in a plane; thus a line ($D_T=1$) has a lower topological dimension than a plane ($D_T=2$). Similarly, a plane can be contained in a volume; thus a volume has a greater topological dimension ($D_T=3$) than a plane. Fractal dimensions are also measures of the amount of space occupied, but they do not have integer values. The following example illustrates the difference between D and D_T. Any curve, such as those shown in Fig. 2, can be contained in a plane; thus $D_T=1$. However, the complex curves (Fig. 2b, c) have a much greater length than do simple curves (Fig. 2a); therefore, these convoluted and involuted curves have $D>1$. As curves becomes increasingly complex (i.e. plane-filling) in a self-similar fashion, D continues to increase, approaching an upper limit at the topological dimension of a plane (since no curve can take up more space than a plane). Thus, the fractal dimensions of all plan-view shapes of self-similar objects are in the range: $1<D<2$. The method by which fractal dimension is calculated is described below.

Bruno et al. (1992) showed that the flow margins of both endmember types of basaltic lavas (a'a and pahoehoe) are fractal, with the scale of self-similarity extending from about 0.5 m to over 2 km. This suggests that the processes that control the shapes of basaltic flows at a small (say, 1 m) scale are dynamically similar to the processes that control flow shapes at a 10 m or 100 m scale. For pahoehoe flows, this implies that the same factors that control the outbreak of a small toe control the outbreak of a larger eruptive unit. For a'a flows, which have crenulation-like features superimposed upon larger flow lobes, self-similarity implies that the same factors that cause these crenulations to form (presumably related to differential shear stress) are also responsible for forming the lobes themselves; i.e. the lobes are large-scale crenulations. Kilburn (1990) made a similar point in describing the fractal properties of the surfaces of a'a flows. Also, Bruno et al. (1992) discovered that the margins of a'a and pahoehoe flows have different fractal dimensions. Pahoehoe margins have higher D (typically ≥ 1.15) than do a'a flows (usually ≤ 1.09). This is consistent with our observation that outlines of pahoehoe margins are qualitatively different from a'a margins (Fig. 3); pahoehoe margins tend to have many more embayments and protrusions than the more 'linear' a'a margins.

These differences in geometry do not reflect differences in composition, but rather differences in rheology and emplacement mechanisms. Whether an erupting basalt becomes a'a or pahoehoe depends on a critical relationship between volumetric flow rate (largely controlled by effusion rate and ground slope), effective viscosity and shear strength (Shaw et al. 1968; Shaw 1969; Peterson and Tilling 1980; Kilburn 1981). Pahoehoe flows are associated with low terminal volumetric

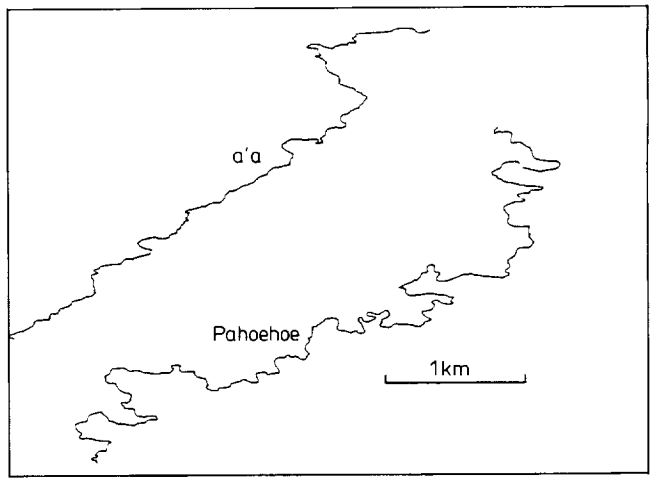

Fig. 3. Digitized outlines of typical a'a and pahoehoe flows from the 1935 eruption of Mauna Loa volcano. The pahoehoe margin is more convoluted than the a'a margin, and would be expected to have a higher D (following Bruno et al. 1992)

flow rates (typically $<10\ m^3/s$ for Hawaiian eruptions) and/or fluid lavas (Rowland and Walker 1990). They tend to be thin (<2 m) and advance with a smooth rolling motion (Cas and Wright 1987). Pahoehoe flows are formed in compound flow fields composed of numerous thin overlapping units. In contrast, a'a flows form at higher terminal flow rates. They are generally associated with higher effusion rates (typically $>10\ m^3/s$ for Hawaiian eruptions) and/or viscous lavas (Rowland and Walker 1990). A'a flows are generally thicker (typically a few meters), and have massive interiors and clinkery exteriors. Unlike most pahoehoe flows, they are erupted as a single unit. A'a and pahoehoe lavas also differ in mode of transport. Lava tubes can play crucial roles in transport of pahoehoe lavas, enabling flow over long distances with small radiative heat losses; a'a lavas typically flow in open channels. All of these differences in terminal flow rates, flow styles and emplacement mechanisms lead to different fractal dimensions for a'a and pahoehoe flows.

One of the objectives of investigations of flow morphology is to determine rheological properties and perhaps lava-flow composition, particularly SiO_2 and volatile content. So, in addition to basalts, we have studied more silicic flows with SiO_2 contents ranging from 52 to 74 wt %. Silicic flows can erupt as single-flow units characterized by a blocky morphology. They are also often associated with channel formation. Thus, in terms of both morphology and emplacement mechanism, some high-silica flows are similar to a'a flows and different from pahoehoe flows. We have found that higher silica contents and the accompanying increase in viscosity and presumable yield strength lead to qualitative as well as quantitative differences in plan-view shapes. Figure 4a shows a basaltic a'a flow, characterized by fairly linear margins, superimposed upon which are small-scale features that resemble crenulations. Figure 4b (basaltic andesite) has finger-like lobes, hundreds of meters in diameter, and appears less 'linear'. Like basaltic a'a, this basaltic andesite has a crenulated appearance. Figure 4c (andesite) also has multiple lobes. Here, the lobes appear shorter, stubbier and wider (approaching 1 km), and the crenulations appear to be absent. Figure 4d (dacite) is characterized by the highest silica content. Here the lobes are still wider (>1 km) and protrude less from the main mass of the lava flow, causing the flow to assume a more bulbous appearance. We note that silica content is just

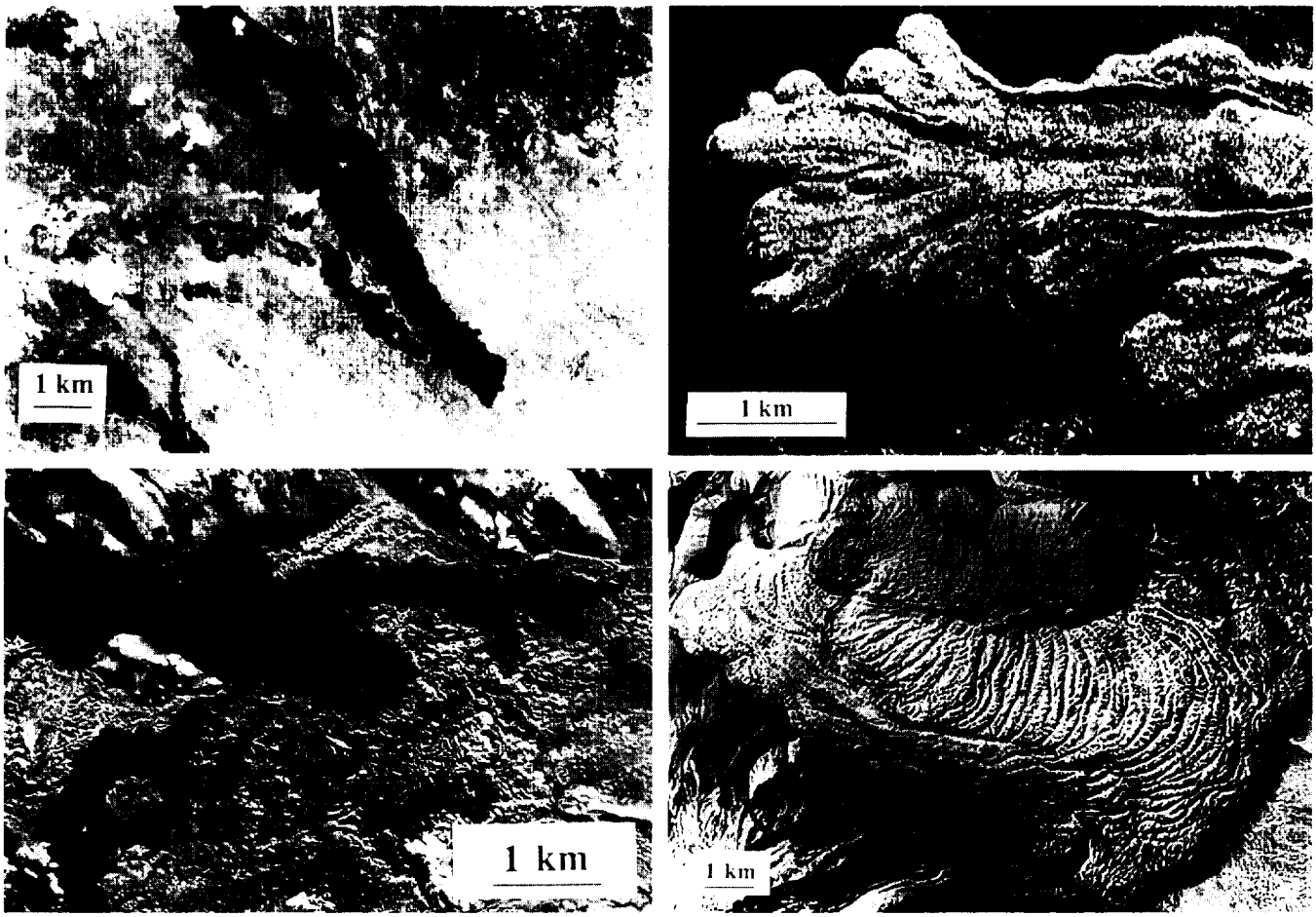

Fig. 4a–d. Plan-view shapes of lava flows of various compositions (in order of increasing silica content): **a** basalt (Galapagos Islands); **b** basaltic andesite (Hekla, Iceland); **c** andesite (Mount Shasta, US); **d** dacite (Chao, Chile). As silica content increases, flow lobes tend to widen, thicken and protrude less from the main mass of the lava flow, and the smaller-scale features become suppressed

one controlling factor on plan-view shape; there are many other controlling factors (e.g. overall volume, volatile content, eruption rate). Nevertheless each range of silica content (basalts, basaltic andesites, andesites, and dacites/rhyolites) appears to show qualitative differences in plan-view shape. In this paper, we quantify the effect of rheology on perimeters of lava flows using fractal analysis. Our objective is to define quantitative parameters that vary with rheology, which in combination, can be used to remotely distinguish flow types.

Methodology

The fractal analysis employed in this study uses three quantitative parameters: correlation coefficient (R^2), fractal dimension (D), and quadratic coefficient (a). These parameters are all calculated in accordance with the 'structured-walk' method (Richardson 1961). Alternative methods include 'equipaced polygon', 'hybrid walk' and 'cell-count' methods; these are discussed in detail in Longley and Batty (1989). We selected the structured-walk method because it can be readily applied, both in field measurements and from remote-sensing images. According to the structured-walk method, the apparent length of a lava-flow margin is measured by walking rods of different lengths along the margin. For each rod length (r), flow margin length (L) is determined according to the number of rod lengths (N) needed to approximate the margin; that is, $L = Nr$. By plotting log L vs log r (called a 'Richardson plot', after Richardson 1961), fractal behavior can be determined.

Calculating correlation coefficient (R)

A linear trend on a Richardson plot indicates the data form a fractal set, indicating self-similarity over the range of rod lengths used. Our criterion for linearity (i.e. fractal behavior) is an R^2 value exceeding 0.95, where R is the correlation coefficient of the linear least squares fit. This criterion is chosen somewhat arbitrarily, but follows that used by Mueller (1987). Care was taken to ensure that the data array did not artificially flatten out at long rod lengths as a result of choosing rod lengths that are so large such that they approach the length of the object. One can avoid this problem altogether by letting r approach the length of the object (that is, letting N approach 0) and plotting all the data on a Richardson plot. One can then visually select the linear portion of the curve and fit a least squares line to the selected segment. Although we have found this technique suitable in measurements of lava flows taken from aerial photographs, it is quite impractical in the field, as it would involve a large number of time-consuming measurements. We have found that choosing our longest rod length such that it can be placed at least five times along a flow margin (i.e. $N = 5$ is a minimum value) is sufficient to prevent this artifact from compromising our results.

Calculating fractal dimension (D)

The fractal dimension of a curve (such as a lava-flow margin) is a measure of the curve's convolution, or deviation from a straight line. The fractal dimension (D) can be calculated as:

$$D = 1 - m,$$

where m is the slope of the linear least squares fit to the data on the Richardson plot (see Turcotte 1991 for derivation and more detailed discussion). Because lava-flow margins are characterized by embayments and protrusions and smaller rods traverse more of these features, L increases as r decreases. Thus, the Richardson plot has a negative slope ($m < 0$) and $D > 1$.

Calculating quadratic coefficient (a)

In the above discussions of calculating fractal dimensions and correlation coefficients, the data on the Richardson plot are fit with a least squares line. Alternately, the data can be approximated by a second-order least squares fit and the quadratic coefficient (a) can provide insight into fractal tendency. An ideal fractal would be expected to have $a = 0$. (We tested this methodology on an ideal, computer-generated fractal and found $a = 0.002$). A negative value of a on a Richardson plot (concave-downward) translates to an increase in slope with increasing rod length, indicating a relative lack of small-scale features. A positive value of a (concave-upward) correlates with a decrease in slope with increasing rod length, or a relative lack of large-scale features.

Field measurement technique

We applied our methodology to lava-flow margins both in the field and on aerial photographs and other images. The field technique requires two people, a tape measure, and measuring rods of various lengths. We use wooden dowels to define the smaller rod lengths (1/8, 1/4, 1/2 and 1 m) and lightweight chains to define the longer rod lengths (2, 4, 8 and 16 m). First, we isolate a section of flow margin to be measured and, somewhat arbitrarily, choose a point along the margin as the starting point. When the selected section of flow margin is sufficiently long to permit, the measurement begins with one person holding one end of the 16 m chain at the starting point (a). A second person walks along the flow margin until the other end of the taut chain exactly intersects the outline. This new point (b) becomes the next starting point. Now, as the second person holds the end of the 16 m chain fixed over point b, the first person walks along the boundary until the next intersection point (c) is found. This process continues until a given number of lengths (N) are measured, and the ending point is marked. To maximize accuracy, the measurement is replicated using the same

Table 1. Directional analysis. N values obtained by replicating field measurement in opposite direction

r (meters)	N_1	N_2
16	5.00	5.02
8	11.52	10.81
4	26.73	25.55
2	63.61	63.63
1	140.10	140.19

chain length, but this time the persons walk in the opposite direction (from the ending point to the starting point). We have found that the N values from both directions match well (Table 1). The results (N) are averaged and L (in meters) is calculated as $L=Nr$. Ideally, this first length calculation (L_1) will be based on five lengths of a 16 m chain, so $L_1=80$ m.

We then recalculate the length of the same segment (L_2), using a chain half of the original length ($r=8$ m). Since the 8 m chain will, in all probability, record some undulations in the flow margin that were not encountered by the 16 m chain, $L_2>L_1$, implying $N_2>10$. Note that it is possible (and likely) that N_2 will be a fraction. We continue dividing the chain length by two and repeating the procedure until at least five measurements of L have been made using five different rod lengths, i.e. the Richardson plots have a minimum of five data points.

For sufficiently long flow-margin segments, these data points generally correspond to chain lengths of 1, 2, 4, 8, and 16 m. In some cases, we included an additional rod length of 0.5 m. For shorter flow-margin segments that cannot accommodate five lengths of a 16 m chain, the first (longest) chain length we chose is the longest chain length that can be walked along the flow margin at least five times. In these cases, rod lengths smaller than 1 m are necessarily used to meet the minimum requirement of five measuring rods/chains, separated by a factor of two in length. The smallest rod lengths used were 0.25 m for a'a flows and 0.125 m for pahoehoe flows.

Error and variation analyses of field measurement technique

We conducted analyses, based on field measurements, to confirm both the field measurement technique's precision ('error analysis') as well as its applicability to the entire flow margin ('variation analysis'). To assess the precision, we conducted five replicate measurements of a typical Hawaiian pahoehoe margin: a portion of the 1972 Mauna Ulu pahoehoe flow (Kilauea Volcano). We began each measurement at the same starting point, and measured off five lengths of a 16 m chain. Therefore, the ending points of each measurement did not necessarily coincide, but instead were chosen such that $L_1=80$ in each case. Each measurement consisted of five data points, corresponding to chain lengths of 1, 2, 4, 8 and 16 m. The results of this error analysis are summarized in Table 2. Note the negligible variance of D: $\sigma=0.008$. Although this error analysis implies that the technique is precise, it does not suggest that the calculated D of a given flow-margin segment is representative of the entire flow. Different segments of a flow margin may have different fractal dimensions, and this error analysis does not measure this segment-to-segment variation. Therefore, we performed an additional analysis on the 1972 Mauna Ulu pahoehoe flow to rigorously study variation along a flow margin. We measured D of seven adjacent segments of a flow margin in the field, with each segment defined as five lengths of a 16 m chain ($L_1=80$). These results, summarized in Table 3, show a significantly larger variation, with $\sigma=0.05$.

Table 2. Error analysis (field data of 1972 Mauna Ulu pahoehoe, segment 1)

Trial number	D	R^2
1	1.163	0.980
2	1.173	0.977
3	1.177	0.988
4	1.182	0.980
5	1.182	0.990
Mean D value:	1.175	
Standard deviation:	0.008	

Table 3. Variation analysis (field data of 1972 Mauna Ulu, pahoehoe)

Segment number	D	R^2
1 (avg.)	1.175	0.987
2	1.207	0.958
3	1.315	0.960
4	1.186	0.997
5	1.183	0.984
6	1.161	0.980
7	1.185	0.956
Mean D value:	1.202	
Standard deviation:	0.052	

Photographic measurement technique

A form of the same 'structured-walk method' was utilized to determine fractal dimensions of lava flows from aerial photographs and radar images, at scales ranging from 1:6000 to 1:70000. We tried to use flow margins in the centers of the images to avoid distortion.

The margins were digitized and the fractal dimensions calculated using the EXACT algorithm (Hayward et al. 1989). Computerization facilitates changing the rod lengths in small increments, improving the precision of the calculated D. We used 30 rod lengths, equally spaced on a log scale. (Using more than 30 rod lengths did not significantly improve the calculated D.)

Consistent with the field methodology, the minimum flow-margin segment included in the aerial photographic data set corresponds to N = 5 for the longest rod length, and fractional N-values were permitted for subsequent rod lengths. The actual length of this longest rod depends on the scale of the image, and ranges up to 2.4 km. The minimum rod length was chosen to be sufficiently large as to exceed both the noise inherent in the digitization process as well as the spatial resolution of photographic images.

Error and variation analyses of photographic measurement technique

Analogous with our analyses of the field technique, we conduct error and variation analyses to confirm the photographic measurement technique. Since this technique is computerized, it is perfectly reproducible; every measurement taken from a given starting point will, after a certain amount of rod lengths are measured, result in the exact same ending point. Thus, any error analysis of fractal dimension would necessarily yield $\sigma = 0$. In order to assess variation of fractal dimension among different segments of flow margin, we select the longest flow margin in the photographic database (Hell's Half Acre, pahoehoe). We divide this margin, which contains over 8000 data points, into seven overlapping flow-margin segments. Each of these segments contains 2000 points and overlaps adjacent segments by 1000 points. Thus segments 1, 3, 5, and 7 are non-overlapping, as are segments 2, 4 and 6. To be consistent with our field variation analysis, we would ideally like to have seven non-overlapping flow segments. However, data limitations prevent this. The results of this analysis, summarized in Table 4, show a comparable variation, with $\sigma = 0.04$.

Data

The database consists of 55 lava flow margins (or segments thereof). The selected margin may be of an individual eruptive unit or a compound flow field. In choosing suitable candidates for measurement, we used the following 'simple-case' criteria: (1) The margin is continuous, well-preserved and unambiguous (e.g. not obscured by forest or younger flows); (2) It is unaffected by external controls, such as a steep ground slope or preexisting topography; (3) The segment is representative of the entire margin. We categorize the analyzed flows based on composition, separating the basalts from the more silicic flows. We further divide the more silicic flows based on silica content. This database is an extension of that considered by Bruno et al. (1992), which included 28 basaltic lava flows.

Table 4. Variation analysis (photographic data of Hell's Half Acre, pahoehoe)

Segment number	D	R^2
1	1.204	0.970
2	1.263	0.953
3	1.243	0.936
4	1.188	0.954
5	1.177	0.969
6	1.218	0.960
7	1.270	0.953
Mean D value:	1.223	
Standard deviation:	0.036	

Basaltic lava flows

This analysis of basaltic lava flows is based on two types of data: (1) field studies of 27 lava flows on Kilauea, Mauna Loa and Hualalai volcanoes on Hawaii. These flows have different morphologies, and include seven a'a, 16 pahoehoe and four 'transitional' flows, i.e. flows with morphologies intermediate between a'a and pahoehoe; (2) aerial photographs of 18 lava flows in Hawaii, the western US, Iceland, and the Galapagos Islands. These flows include eight pahoehoe and ten a'a. No transitional flows are included in the photographic database. Scales of photographs range from 1:6000 to 1:60000, which determine the rod lengths which range from 12 m to 2.4 km. Including the field data, the scale extends down to 0.125 m for pahoehoe flows and 0.25 m for a'a flows. The database for basaltic flows is summarized in Table 5a.

Silicic lava flows

This analysis of silicic lava flows is based exclusively on data obtained from aerial photographs and radar images; no field data have been taken to date. The database, summarized in Table 5b, consists of ten flows with silica contents ranging from 52 to 74%. We divide these flows into two categories based on silica content: basaltic andesites (SiO_2: 52–58%) and more silicic flows (SiO_2: 61–74%), the latter being primarily dacites and rhyolites. These images have scales ranging from 1:8250 to 1:70000, which determine the lengths of rods used (10 m–4.5 km).

Results and discussion: basaltic lava flows

Basaltic lava flow margins are fractals

Our preliminary results (Bruno et al. 1992) indicated that both a'a and pahoehoe flow margins are fractals within the range of scale studied (r: 0.5 m–2.4 km). Richardson plots are linear (Fig. 5), demonstrating self-similarity. The present analysis confirms that conclusion based on a larger database (45 flows) and over a wider range of scale (r: 0.125 m–2.4 km). Furthermore, transitional flows have also been shown to be fractal. The only cases where the margins of basaltic

Table 5a. Database of basaltic flows

Flow description	Flow type	D	R^2	Data type	Substrate (field data only)
Kilauea Volcano, Hawaii					
1971 Mauna Ulu	pahoehoe	1.19	0.962	field	ash
1972 Mauna Ulu	pahoehoe	1.20 (avg)	0.994	field	pahoehoe
1972 Mauna Ulu	pahoehoe	1.18	0.973	field	pahoehoe
1972 Mauna Ulu	pahoehoe	1.21	0.987	field	pahoehoe
1972 Mauna Ulu	pahoehoe	1.20	0.982	field	pahoehoe
1972 Mauna Ulu	a'a	1.05	0.990	field	pahoehoe
1972 Mauna Ulu	a'a	1.06	0.988	field	pahoehoe
1974 Mauna Ulu	pahoehoe	1.15	0.963	field	pahoehoe
1974 Mauna Ulu	transitional	1.10	0.975	field	pahoehoe
1974 Mauna Ulu	transitional	1.12	0.977	field	pahoehoe
1974 Mauna Ulu	a'a	1.07	0.987	field	pahoehoe
1974 Mauna Ulu	a'a	1.09	0.963	field	pahoehoe
1974 Mauna Ulu	a'a	1.08	0.965	field	pahoehoe
1977 Pu'u O'o	a'a	1.05	0.967	photo	
1982 Kilauea	pahoehoe	1.21	0.989	field	ash
1990 Pu'u O'o	pahoehoe	1.18	0.995	field	pahoehoe
Mauna Loa Volcano, Hawaii					
prehistoric, nr Saddle Rd	pahoehoe	1.23	0.988	field	a'a
prehistoric, nr Pu'u Ki	pahoehoe	1.23	0.997	field	a'a
prehistoric, nr Pu'u Ki	pahoehoe	1.12	0.954	field	pahoehoe
1843 Mauna Loa	a'a	1.11	0.972	photo	
1843 Mauna Loa	pahoehoe	1.15	0.969	field	pahoehoe
1852 Mauna Loa	pahoehoe	1.13	0.992	photo	
1855 Mauna Loa	pahoehoe	1.19	0.960	photo	
1855 Mauna Loa	pahoehoe	1.17	0.986	field	pahoehoe
1855 Mauna Loa	pahoehoe	1.19	0.979	field	a'a
1855 Mauna Loa	transitional	1.09	0.961	field	a'a
1859 Mauna Loa	a'a	1.07	0.965	photo	
1859 Mauna Loa	pahoehoe	1.14	0.970	field	a'a
1881 Mauna Loa	pahoehoe	1.17	0.970	photo	
1899 Mauna Loa	a'a	1.13	0.981	photo	
1935 Mauna Loa	a'a	1.08	0.973	photo	
1935 Mauna Loa	pahoehoe	1.20	0.956	photo	
1935 Mauna Loa	pahoehoe	1.15	0.988	field	a'a
1942 Mauna Loa	a'a	1.07	0.973	photo	
Hualalai Volcano, Hawaii					
1800 Hualalai	a'a	1.06	0.968	photo	pahoehoe
1800 Hualalai	transitional	1.15	0.992	field	pahoehoe
1800 Hualalai	a'a	1.09	0.967	field	pahoehoe
1800 Hualalai	a'a	1.08	0.995	field	pahoehoe
Non-Hawaiian Volcanoes					
Hell's Half Acre, Idaho	pahoehoe	1.21	0.981	photo	
Volcano Peak, California	pahoehoe	1.23	0.963	photo	
Fernandina, Galapagos	a'a	1.07	0.972	photo	
Fernandina, Galapagos	a'a	1.09	0.952	photo	
Fernandina, Galapagos	a'a	1.05	0.985	photo	
Krafla, Iceland	pahoehoe	1.16	0.971	photo	

flows are not fractal are on steep slopes. In these cases where the margin is externally controlled by a steep ground slope, the margin becomes more linear, with fewer convolutions.

The fractal behavior of pahoehoe and a'a flows might be predicted by their basaltic composition. Low viscosities of the order of 1000 Pa-s for typical eruption temperatures of 1150° C, coupled with a negligible yield strength for most basalts, offers no obstacle to prevent self-similar features from being formed on a wide range of scales. We note that at some small scale below the detection limit of this study, fractal behavior will eventually break down due to material properties.

Pahoehoe and a'a have different D

We find that over a wide range of geographic locations (Hawaii, Iceland, western US, Galapagos Islands), basaltic lavas divide into two populations with regard to their fractal dimensions. A'a flows generally have D

Table 5b. Database of silicic flows

	Flow description	SiO_2 (%)	Flow type	Scale of image	Reference
1	Andes Mountains	52	Bas. Andesite	1:27000	Thorpe et al. (1984)
2	Andes Mountains	52	Bas. Andesite	1:13500	P Francis (personal communication)
3	1980 Hekla, Iceland	55	Bas. Andesite	1:8250	Gudmundsson et al. (1991)
4	1991 Hekla, Iceland	55	Bas. Andesite	1:21500	Gudmundsson et al. (1991)
5	SP Flow, Arizona	57	Bas. Andesite	1:36000	Ulrich and Bailey (1987)
6	Lava Park Flow, California	61	Andesite	1:30000	Smith and Carmichael (1968)
7	Ludent, Iceland	65	Dacite	1:8250	Nicholson (personal communication)
8	1104 Hekla, Iceland	65	Dacite	1:8250	Sigmarsson (personal communication)
9	Chao, Chile	66	Dacite	1:70000	Guest and Sanchez (1969)
10	Glass Mountain, California	74	Rhyolite	1:12000	Eichelberger (1975)

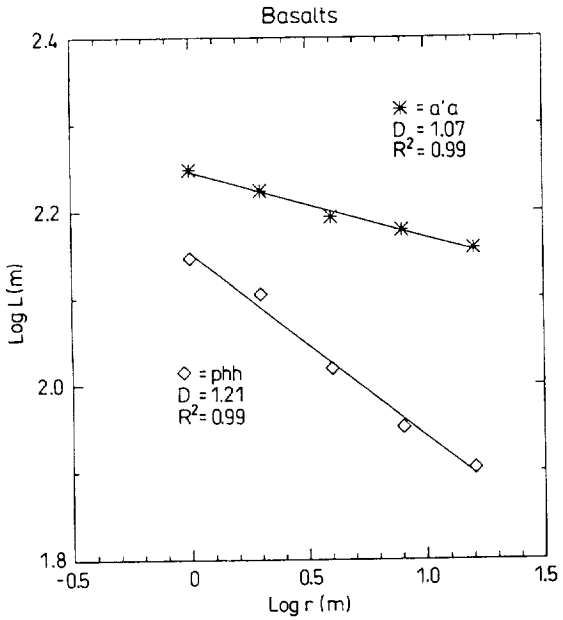

Fig. 5. Richardson plots of typical a'a and pahoehoe flows, in meters, based on field data. High R^2 values (>0.95) indicate fractal behavior. The more convoluted margins of pahoehoe flows translate to higher D

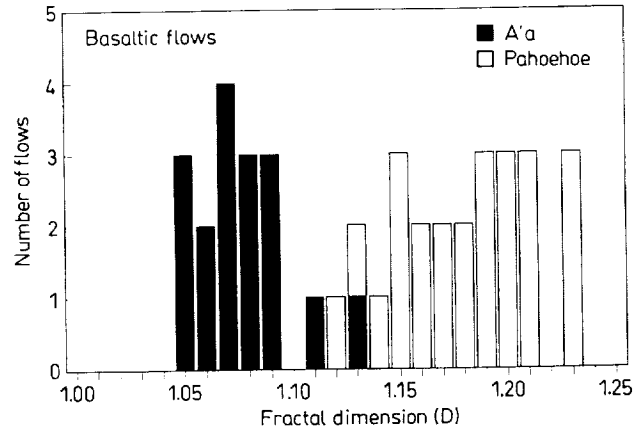

Fig. 6. Histogram of D values of a'a and pahoehoe flows based on field and photographic data. Both field and photographic measurements show pahoehoe flows have higher D than a'a flows. Transitional flows (not shown) tend to have intermediate D

ranging between 1.05 and 1.09 whereas pahoehoe flows typically have D ranging between 1.15 and 1.23. Figure 6 summarizes our results for basaltic flows. Most (12 of 14) of the Hawaiian a'a flows have D between 1.05 and 1.09; all have D between 1.05 and 1.13. Most Hawaiian pahoehoe flows (18 of 21) have D between 1.15 and 1.23; all have D between 1.12 and 1.23. The two pahoehoe flows in the western US yield measurements of 1.21 and 1.22, consistent with the range of Hawaiian pahoehoe flows. Similarly, the Krafla, Iceland basalt (pahoehoe) falls into the Hawaiian pahoehoe range, with a fractal dimension of 1.16. The three Galapagos flows measured, all a'a, yield D values of 1.05, 1.07 and 1.09, in agreement with the range of Hawaiian a'a flows. This is good evidence that regardless of the exact nature of the eruption, the pahoehoe flows consistently have higher D than a'a flows.

By definition, fractals should have constant ranges of fractal dimensions, regardless of the rod lengths used to measure D. Thus, if lava flows are fractals over the range of scale studied, the fractal dimensions obtained at the field scale (0.125–16 m) should be similar to the range of fractal dimensions obtained at the aerial photographic scale (12 m–2.4 km) for a'a as well as pahoehoe. This is confirmed by our results. All seven a'a flows measured in the field have D between 1.05 and 1.09 (Fig. 6), the same range we find for photographic data of a'a flows (Fig. 6). All 16 pahoehoe field measurements have D between 1.12 and 1.23, compared with a range of 1.13–1.23 for photographic data of pahoehoe flows.

For three flows (all pahoehoe), we measured margins of the same flow in the field and from aerial photographs. The fractal dimensions as measured from aerial photographs are 1.19 (1855 Mauna Loa), 1.14 (1859 Mauna Loa) and 1.20 (1935 Mauna Loa). Field measurements yielded corresponding D of 1.17, 1.16 and 1.15, respectively. These variations in D are within the variation of Table 3, and indicate fractal behavior.

Flows that we have determined to be transitional between a'a and pahoehoe based on field observations tend to have intermediate fractal dimensions, as might be expected. Of the four field measurements of transitional flows, three have D between 1.09 and 1.12; the fourth has a slightly higher D of 1.15.

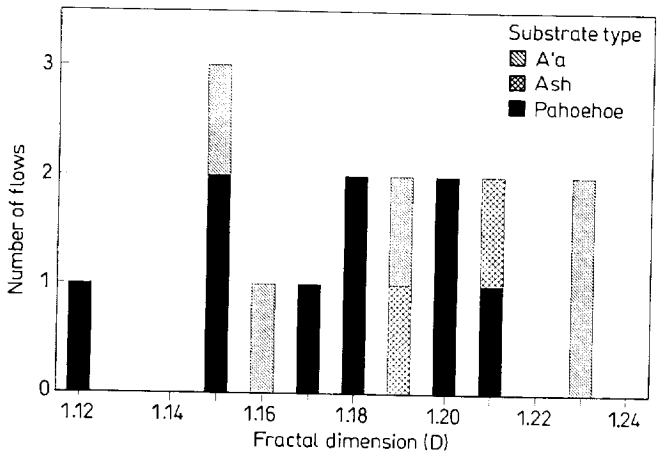

Fig. 7. Histogram of D values of pahoehoe flows on three different substrates – preexisting a'a or pahoehoe flow, or ash – based on field data. There is no apparent correlation between D and substrate type

One might expect that the fractal dimensions of flow margins would be affected by the nature of the substrate over which they flowed. A pahoehoe margin might be different on a preexisting a'a flow compared to a preexisting pahoehoe flow. However, a detailed analysis shows that D values are unaffected by differences in substrate. We took 16 field measurements of Hawaiian pahoehoe flows. Some of these lavas flowed upon preexisting a'a lava flows (5), others upon preexisting pahoehoe flows (9), still others atop ash deposits (2). Figure 7 shows the lack of correlation between D and substrate for these 16 flows. In one case (1855 Mauna Loa pahoehoe), we performed a controlled experiment on the effect of substrate on D. We measured D in one location where this pahoehoe flowed over a preexisting pahoehoe, and again nearby (within 100 m), where the same flow covered an a'a substrate. The D values obtained for this flow overlying pahoehoe and a'a substrates (1.17 and 1.19, respectively) are well within the observed variation of D along a flow margin with a constant substrate (see Table 3).

Clearly, a pattern emerges for the fractal dimensions of terrestrial basaltic lava flows. Regardless of geographic location, lengths of rods used, or substrate material, pahoehoe flow margins consistently have higher D than a'a flow margins within the range of scale studied. This is consistent both with the preliminary results of Bruno et al. (1992) and also the observation that the outlines of pahoehoe and a'a flows are qualitatively different.

A note about topographically controlled flows

Topographically controlled flows have been excluded from this analysis because these external controls can have a significant effect on D. Positive topography (e.g. hills) may deflect or bifurcate flows, increasing the degree of flow-margin convolution and therefore increasing D. Negative topography (e.g. channels) serves to confine or channelize flows, causing the margin to become more linear and thus decreasing D. In many cases, these external controls interfere with the development of self-similar features, and prevent fractal behavior. Similarly, we have found fractal behavior to break down, with an accompanying decrease in D, on steep (>15–28°) slopes (see Table 6). This tendency toward nonfractal behavior as the gravity-driven force on the flow increases is consistent with the results presented in Baloga et al. (1992).

Table 6. Slope analysis. Effect of slope on fractal properties of 1972 Mauna Ulu a'a flow (field data)

Flow Description	Flow type	D	R^2	Slope
1972 Mauna Ulu	a'a	1.046	0.990	11.6°
1972 Mauna Ulu	a'a	1.055	0.988	14.7°
1972 Mauna Ulu	a'a	1.023	0.778	27.8°

Implications for flow dynamics

The fractal properties of lava flows may offer insight into the dynamics of flow emplacement because fractals reflect nonlinear processes (e.g. Campbell 1987). We have made a preliminary evaluation of the nonlinear aspects of flow dynamics to obtain a qualitative indication of the tendency toward fractal behavior. Following earlier fluid dynamic models (e.g. Baloga and Pieri 1986; Baloga 1987), we depict variations in the free surface of a lava flow as due to a balance between a gravitational transport term and the fluid dynamic ('magmastatic') pressure gradient. Baloga et al. (1992) define two dimensionless parameters (p and q) to describe the relative importance of these two influences. The parameter p is the ratio of the pressure gradient to gravitational terms; the parameter q is an absolute measure of the gravitational force on the flow. Baloga et al. (1992) developed a governing equation for the three-dimensional surface of a lava flow during emplacement, based on simplifying assumptions:

$$\partial h/\partial t + q\,h^2(\partial h/\partial x) = p\,q\,\partial/\partial y[h^3(\partial h/\partial y)]$$

where

$$p = \cot\theta\, h_0 L/(3w^2)$$

$$q = g\sin\theta\, h_0^2 T/(\nu L)$$

and where x and y are the downstream and cross-stream directions respectively, h = flow thickness, t = time; h_0, L, w and T are scales for thickness, length, width and time, respectively; θ = slope, ν = kinematic viscosity and g = gravitational acceleration.

By assuming $\partial h/\partial t$ is on the order of 1, Baloga et al. (1992) evaluated this equation for selected values of p and q (Fig. 8). High p values (right column of the matrix) indicate the magmastatic pressure gradient is important relative to gravity. Low q values (top row of matrix) indicate a weak gravitational term. Thus, in case 1c (large p, small q), the gravitational term is the least important, both relatively (to the pressure gradient) and absolutely, and the magmastatic pressure

	$p \ll 1$	$p = 1$	$p \gg 1$
$q \ll 1$	**Case 1a** $\partial h/\partial t = 0$	**Case 1b** $\partial h/\partial t = 0$	**Case 1c** Assume $pq = 0(1)$ $\partial h/\partial t = \partial/\partial y[h^3(\partial h/\partial y)]$
$q = 1$	**Case 2a** $\partial h/\partial t + h^2(\partial h/\partial x) = 0$	**Case 2b** $\partial h/\partial t + h^2(\partial h/\partial x) = \partial/\partial y[h^3(\partial h/\partial y)]$	**Case 2c** $0 = \partial/\partial y[h^3(\partial h/\partial y)]$
$q \gg 1$	**Case 3a** Assume $pq = 0(1)$ $h^2(\partial h/\partial x) = 0$	**Case 3b** $h^2(\partial h/\partial x) = \partial/\partial y[h^3(\partial h/\partial y)]$	**Case 3c** $0 = \partial/\partial y[h^3(\partial h/\partial y)]$

Fig. 8. Matrix of special cases of the governing equation for selected values of p and q, obtained by assuming $\partial h/\partial t$ is on the order of 1. Some of the equations in the matrix are linear; others are nonlinear. The linear equations would not be expected to produce fractals, whereas the nonlinear equations could be expected to produce fractals. See text for details

gradient dominates. Thus, since the lava flow is being largely driven by internal fluid dynamic forces in case 1c, we predict that this combination of p and q is likely to produce fractal behavior. As expected, the resulting diffusion equation is explicitly nonlinear.

For the same q ($q \ll 1$), consider the cases corresponding to p values that are low (case 1a) and moderate (case 1b). Both of these equations are linear, and would therefore not be expected to produce fractals. Since p is proportional to the ratio of magmastatic pressure gradient to gravitational driving force, this has important implications for the effect of gravity on fractal behavior. When gravity plays a non-negligible role (small or moderate p), the matrix predicts that the lava-flow margin would not be fractal. This is consistent with our field observations on Hawaii that flow outlines are not fractals when slopes are steep.

Case 2b is nonlinear diffusion with a kinematic transport term. Case 3b is the steady-state nonlinear diffusion equation. These are also likely candidates for producing fractals. Cases 2c and 3c are both nonlinear and are dominated by the pressure gradient term ($p \gg 1$). These cases may be expected to produce fractal behavior, but are difficult to interpret physically.

This analysis suggests that nonlinear processes are common in lava flows, particularly in those cases where the magmastatic pressure gradient influence is significant relative to the influence of gravitational transport. These nonlinear equations are candidates for producing fractals, provided they are physically plausible. Further studies are underway to (1) test this physical plausibility by continued comparison of theoretical prediction and field measurements and (2) extend the underlying physics to include more complex rheologic properties for lava flows of different compositions.

Results and discussion: silicic lava flows

Silicic lava flows are generally not fractals

Silicic lava flows are generally not fractals within the range of scale studied (r: 10 m–4.5 km). Typical Richardson plots for basalt, basaltic andesite, and dacite are shown in Fig. 9. Unlike the basaltic case, the Richardson plots for basaltic andesite and dacite are nonlinear, characterized by relatively low R^2 values. Instead of fractal behavior, these Richardson plots exhibit scale-dependent behavior: longer rod lengths have steeper slopes, most notably for the dacite. Thus, D tends to increase as r increases, contradicting the definition of D as a scale-independent parameter. This breakdown of fractal behavior at increased silica content is presumably related to the higher viscosities and yield strengths, which suppress smaller-scale features and thus prevent self-similarity over a wide range of scales.

Quantifying the effect of silica content on D

We seek to develop parameters that can be used remotely to quantify the effect of increasing silica content on fractal properties by comparing basalts, basaltic andesites, and dacites/rhyolites for two main purposes: (1) to gain insights into yield strength and rheological processes, and (2) to develop a remote-sensing tool that can differentiate flow type based on plan-view shape. Our approach is to use the study of basaltic flows as a benchmark for comparison with the more silicic flows. However, we restrict our basaltic 'benchmark' to a'a flows, which are similar to silicic flows in terms of both morphology and emplacement mechanism.

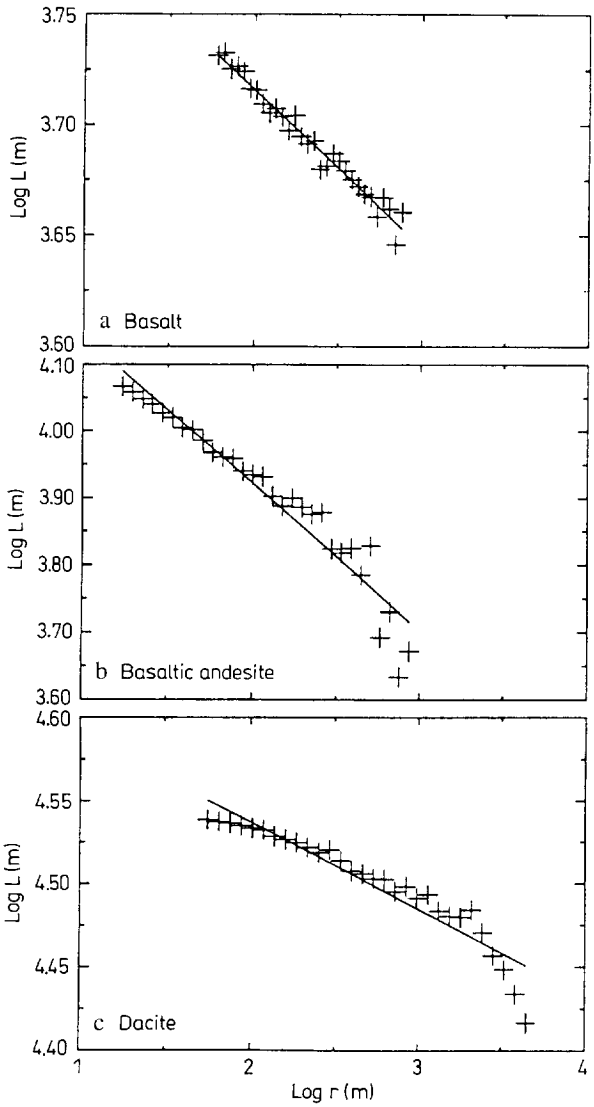

Fig. 9a–c. Richardson plots of representative **a** a'a basalt (Galapagos Islands); **b** basaltic andesite (Hekla, Iceland); **c** dacite (Chao, Chile), based on image data. Note that the data in (a) are closely approximated by a straight line, whereas the data for the higher silica flows (b, c) are not linear

Ideally, we would like to compare D of silicic flows to basaltic flows, to see how D changes with silica content. However, this approach is tricky because, as noted above, silicic flows are generally not fractals; instead D tends to increase with r for the majority of the silicic flows. Hence, the concept of a scale-independent fractal dimension for silicic flows is not valid. However, small regions of log r can be locally fit with a line. Here we introduce the concept of a 'local fractal dimension'. This does not imply the data set is fractal, nor that the local fractal dimension is scale-independent. It simply exploits our observation that select regions of the data can be fit by a line and we can estimate locally the degree of convolution for a selected range of rod lengths. Here we describe two methods used to compare silicic and basaltic flows. Both of these methods are sensitive to – and based on – our observation that silicic flows do not have scale-independent fractal dimensions.

Method 1: disjoint subsets of log r

This method dissects the abscissa of the Richardson plot into disjoint subsets of log r. The specific choice of subsets (summarized in Table 7a) is constrained by the data. Each of these subsets is fit locally by a least squares line; that is, the Richardson plot is fit by a series of lines. For each line, the slope (m) is calculated, and local fractal dimension D is calculated as 1 – m, consistent with our methodology for basaltic flows. Since this method can be used to describe fractals as well as non-fractals, it can be employed to compare basaltic and silicic lava flows.

Figure 10 shows sample Richardson plots of basalt, basaltic andesite and dacite, with the abscissa dissected according to the methodology described above. The data on these plots are the same as shown in Fig. 9; the only difference is the number of lines used to fit the data. Note that for the basalt, the three segments have essentially the same slope. This is consistent with our conclusion that basalts are fractals. Unlike the basalts, the basaltic andesite and dacite show noticeable differences in slope among the various subsets.

By plotting D of these segments vs. log r for the entire database of silicic flows, patterns begin to emerge among the basaltic andesites and the more silicic flows (primarily dacites and rhyolites). The basaltic andesites have roughly the same D values for the first two subsets (Fig. 11). At rod lengths of about 100 m ($\log r = 2$ m), D starts to increase, and the values also have a greater scatter. For the first three subsets of log r, the dacites/rhyolites have D plotting in a rather compact area, showing only negligible differences among the various ranges. At $\log r \sim 2.5$ m, D apparently begins to increase. We can use this technique to distinguish basaltic andesites from the more silicic flows. Both have a general increase in D with longer r, but the basaltic andesites tend to have greater D for each of these categories. Furthermore, the fact that dacites/rhyolites show negligible changes within the first three subsets ($\log r < 2.5$ m), whereas the basaltic andesites only remain relatively constant for the first two

Table 7. Ranges of log r (meters) for **a** Method 1 and **b** Method 2

a	METHOD 1	
		Log r (meters)
	Range 1:	< 1.5
	Range 2:	1.5–2.0
	Range 3:	2.0–2.5
	Range 4:	2.5–3.3
b	METHOD 2	
		Log r (meters)
	Range 1:	1.7–2.8
	Range 2:	1.7–2.5
	Range 3:	1.3–2.0

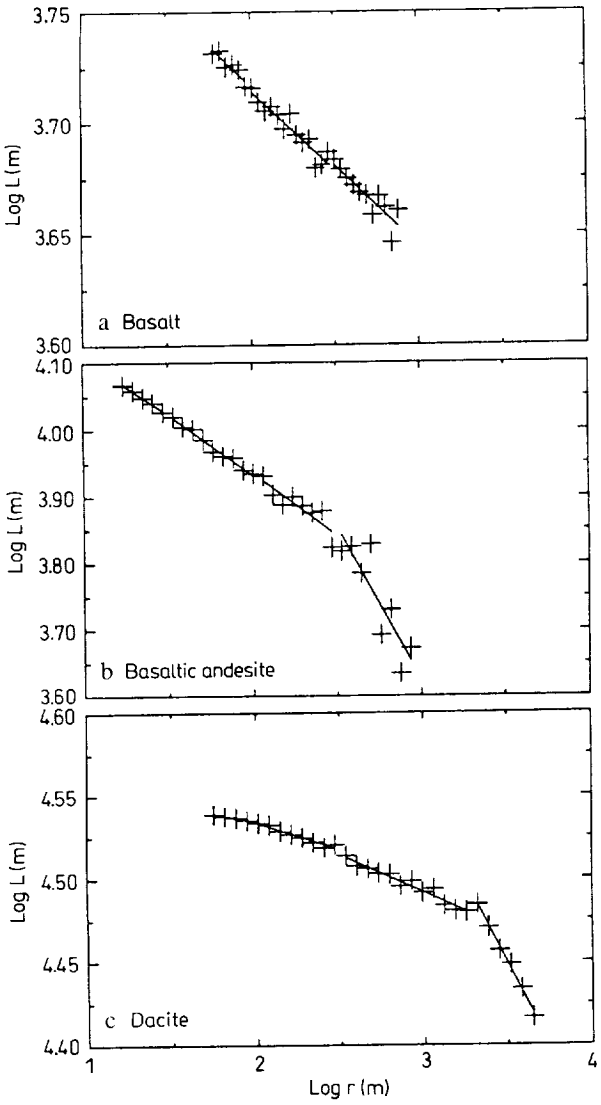

Fig. 10. Dissected Richardson plots of representative samples of **a** a'a basalt (Galapagos Islands); **b** basaltic andesite (Hekla, Iceland); **c** dacite (Chao, Chile), based on photographic data (same data as Fig. 9). Here, the abscissa is dissected into ranges of logr (Table 7a), and each range is locally fit with a straight line. Local fractal dimension is calculated as $D = 1 - m$, where m is the local slope as calculated according to Method 1. From left to right of these Richardson plots (increasing r), these local fractal dimensions are: **a** D = 1.07 for each segment; **b** D = 1.17, 1.19, 1.19, 1.46. (c) 1.02, 1.03, 1.05, 1.20. Note that D values are constant for (a), but not for (b) and (c). See text regarding Method 1

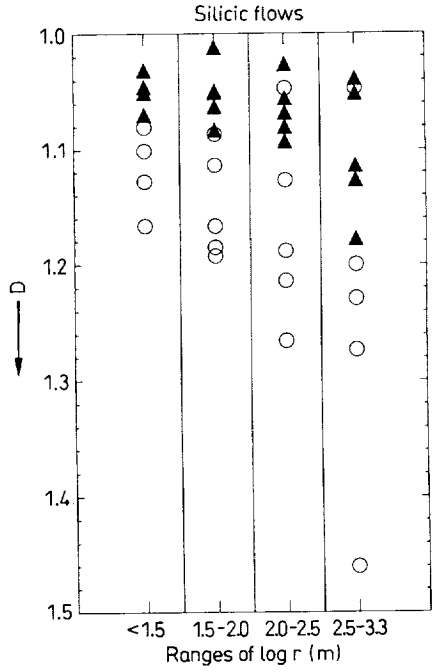

Fig. 11. Summary of 'local fractal dimension' (D) based on photographic data for entire database of silicic flows. Basaltic andesites are shown as *open circles*, whereas dacites and rhyolites are shown as *solid triangles*. Note that D is not a constant function of logr indicating non-fractal behavior

subsets (logr < 2.0 m), is apparent. Figure 11 also emphasizes that D is not a constant function of logr for both basaltic andesites and dacites/rhyolites, indicating scale-dependent (non-fractal) behavior. Fractals such as basalts have relatively constant fractal dimensions across the various subsets. However, a sufficiently large range of logr is needed to discern fractal and non-fractal behavior. Note that a'a basalts and dacites have a similar range of fractal dimensions for the first three categories. Since data limitations often prevent obtaining such a large range of logr, we invoke a second method to differentiate a'a basalts from dacites, described below.

Method 2: overlapping subsets of logr

Like Method 1, this method dissects the abscissa of the Richardson plot into distinct regions of logr. However, it is different from the previous method in two respects. First, the selected ranges (as summarized in Table 7b) of logr are overlapping. Although the exact choice of ranges is again constrained by the data, they were intentionally chosen to overlap. This is to explicitly show the effect of a restricted range of rod lengths on local fractal dimension. For example, by comparing Region 1 (logr: 1.7–2.8 m) and Region 2 (logr: 1.7–2.5 m), we can explicitly see the effect of a restricted range of logr (2.5–2.8 m) on D and R^2. Second, as these regions span a greater range of logr than those in Method 1, we have sufficient data points to fit a second-order least squares curve to the data, in addition to the standard first-order least squares line. In this method, we fit a curve of the form $y = ax^2 + bx + c$, and note the value of the leading (or quadratic) coefficient *a*. In summary, this method compares three quantitative parameters (D, R^2, *a*) for three overlapping ranges of logr.

Applying Method 2 to dacites and rhyolites, we note systematic variation in D, R^2 and *a* with range of rod length. In four out of five cases, the longest rod lengths (Range 1) have the highest D and the lowest

corresponding R^2 values, whereas the shortest rod lengths (Range 3) have the lowest D and the highest R^2 values. Fitting a quadratic curve to Range 1 in each case yields a negative *a*. For Range 3, *a* can be either positive or negative. The D, R^2 and *a* for the dacites/rhyolites provide remarkably consistent results: all suggest scale-dependent (or non-fractal) behavior, characterized by an increase in D with increasing r. We attribute this to the suppression of small-scale features, due to the higher viscosities and yield strengths of silicic flow. We suggest the margin appears 'linear' to a certain range of small rod lengths because the scale of features they would otherwise detect are suppressed. This explains a fractal dimension close to 1 for the shortest range of rod lengths and, as expected, the corresponding R^2 values are quite high. We interpret these results to suggest that the shortest range of rod lengths (log r: 1.3–2.0 m) detects features in the flow margin that are below the limit of self-similarity.

We now present the results of Method 2 applied to basalts (i.e. those basalts which we measured using the ranges of r shown in Table 7b). Fractal dimension and the corresponding R^2 values show no systematic variation with range of rod length. The R^2 values are high, generally exceeding 0.95. The parameter *a* can be positive or negative, is generally close to zero, and again shows no systematic pattern among the various ranges. These results for D, R^2 and *a* for basalts all suggest fractal behavior.

We can use these fractal parameters to remotely differentiate flow types. Basaltic a'a and basaltic andesites can be distinguished primarily by their D values; basaltic andesites generally have higher D (≥ 1.15) than basaltic a'a (D: 1.05–1.09) and are less likely to exhibit fractal behavior. Although dacites/rhyolites and basalts have similar fractal dimensions (1.05–1.10) for extensive ranges of log r, dacites and rhyolites distinctly show non-fractal behavior. Systematic evaluation of D, R^2, and *a* at different range of rod lengths (as done in Method 2) can be used to distinguish dacites and rhyolites from basalts remotely.

There may be a critical value of r, related to silica content, which serves as a boundary for self-similar behavior (i.e. a value of r above which the flow appears fractal). This critical value may be related to lobe dimensions and/or the degree of suppression of smaller-scale features. Note that Fig. 11 shows a marked increase in D for dacites after about log r of 2.5 m ($r = 300$ m). This may be related to the lobe width of dacites, typically hundreds of meters. If so, we would expect the apparent D of basaltic andesites to increase at shorter rod lengths. This may be suggested by Fig. 11 but our database is too small to be conclusive. We believe that a larger database of silicic flows would reveal a critical value of breakdown of fractal behavior related to silica content. The fact that basaltic andesites appear to have relatively constant fractal dimensions up to $\log r = 2$ m while dacites/rhyolites appear to have relatively constant fractal dimensions up to $\log r = 2.5$ m suggests an effect of yield strength which is related to silica content. Our field observations shows that fractal behavior for basalts also breaks down, but at $r < 10$ cm.

The suppression of smaller-scale features in silicic flows implies that nonlinear instabilities are also suppressed inside the flows. Either the sluggish rheology prevents their formation, or it prevents their growth by rapidly damping out feedback mechanisms. The generally non-fractal nature of the margins of silicic flows is consistent with our simplified flow model (Fig. 8). Viscosities of silicic flows are very large, $>10^6$ for basaltic andesites and $>10^8$ for dacites and rhyolites, so q is certainly $\ll 1$. Thus, unless the flows have very large initial pressures, it is likely that their behavior would tend to be linear.

Conclusions

1. Basaltic lava flows are fractals

Bruno et al. (1992) suggested that basaltic lava flows are fractals, with pahoehoe flow margins having higher fractal dimension (1.13–1.23) than a'a flow margins (1.05–1.09). This study, based on a larger database (45 flows) and over a wider range of scale (0.125 m–2.4 km), confirms that earlier conclusion. Richardson plots are consistently linear, characterized by high R^2 values. Furthermore, we have shown that basaltic lava flows having transitional morphologies also exhibit fractal behavior, and tend to have dimensions intermediate between a'a and pahoehoe. This indicates that basaltic lavas, regardless of the emplacement mechanism, exhibit self-similar behavior. We interpret this to suggest that basalts are sufficiently fluid and lack a sizeable yield strength, offering no obstacle to deter the formation of small-scale self-similar features.

2. Silicic flows are generally not fractals

Unlike basalts, silicic lava flows tend to exhibit scale-dependent (non-fractal) behavior within the range of scale studied (r: 10 m–4.5 km). Typical Richardson plots for basaltic andesites and (especially) the more silicic dacites and rhyolites are non-linear. This breakdown of fractal behavior at increased silica content is presumably related to the higher viscosities and yield strengths, which suppress smaller-scale features.

3. Flow dynamics are nonlinear

Our observations that basaltic lava flows have fractal outlines when they are internally controlled yet have non-fractal outlines when they are controlled by gravitational forces are consistent with our theoretical model. An assessment of flow dynamics suggests that nonlinear processes operate for lava-flow emplacement on relatively flat slopes. These nonlinear mechanisms are damped out in silicic flows, leading to non-fractal margins, especially at small rod lengths.

4. *Quantifying the effect of rheology*

One of the primary objectives of this study is to remotely distinguish flow types. We suggest that fractal dimension (or local fractal dimension), correlation coefficient, and quadratic coefficient can be used, in combination, to attain this objective. We define 'local fractal dimensions' for select ranges of log r, and find that D tends to increase with increasing r after certain critical rod lengths are exceeded. We can use local fractal dimension to differentiate basaltic andesites from dacites and rhyolites. Although basaltic a'a and dacites have similar fractal dimensions over a wide range of r, the parameters R^2 and a can be used to remotely differentiate between these flow types.

Acknowledgements. This research was funded by the following National Aeronautics and Space Administration (NASA) grants: NGT 50930 (NASA Graduate Student Researchers Program), NAGW 3684 and NAGW 1162 (NASA Planetary Geology and Geophysics Program). Additional support was provided by the University of Hawaii Project Development Fund and Harold T Stearns Foundation. This manuscript benefited from reviews by H Shaw and G Valentine. Images were kindly provided by Duncan Munro (Galapagos Islands mosaic), Rosaly Lopes-Gautier and Peter Mouginis-Mark (Western US), Peter Francis (Andes) and Thorvaldur Thordarson (Iceland). Paul Lucey and Harold Garbeil provided software support. Many thanks go to Michelle Tatsumura for field assistance. This is IGP Publication No. 764 and SOEST Contribution No. 3578. This work forms part of the PhD dissertation of B Bruno.

References

Baloga S (1987) Lava flows as kinematic waves. J Geophys Res 92:9271–9279

Baloga S, Pieri D (1986) Time-dependent profiles of lava flows. J Geophys Res 91:9543–9552

Baloga S, Taylor GJ, Bruno BC (1992) The character of lava flow margins. Lunar Planet Sci XXIII:57–58

Bruno BC, Taylor GJ, Rowland SK, Lucey PG, Self S (1992) Lava flows are fractals. Geophys Res Lett 19:305–308

Campbell DK (1987) Nonlinear science. Los Alamos Science 15:218–262

Cas RAF, Wright JV (1987) Volcanic successions. Allen & Unwin, London, 528 pp

Crisp J, Baloga S (1990) A method for estimating eruption rates of planetary lava flows. Icarus 85:512–515

Eichelberger JC (1975) Origin of andesite and dacite: Evidence of mixing at Glass Mountain in California and at other circum-Pacific volcanoes. Geol Sci Am Bull 86:1381–1391

Fink JH (1980) Surface folding and viscosity of rhyolite flows. Geology 8:250–254

Fink JH, Fletcher RC (1978) Ropy pahoehoe: Surface folding of a viscous fluid. J Volcanol Geotherm Res 4:151–170

Garcia L (1991) The fractal explorer. Dynamic Press, Santa Cruz, 108 pp

Gudmundsson A, Oskarsson N, Gronvold K, Saemundsson K, Sigurdsson O, Stefansson R, Gislason SR, Einarsson P, Brandsdottir B, Larsen G, Johannesson H, Thordarson Th (1991) The 1991 eruption of Hekla, Iceland. Bull Volcanol 54:238–246

Guest JE, Sanchez J (1969) A large dacitic lava flow in northern Chile. Bull Volcanol 33:778–790

Hayward C, Orford JD, Whalley WB (1989) Three implementations of fractal analysis of particle outlines. Comp & Geosci 15:199–207

Hulme G (1974) The interpretation of lava flow morphology. Geophys J R Astron Soc 39:361–383

Hulme G, Fielder G (1977) Effusion rates and rheology of lunar lavas. Philos Trans R Soc London A285:227–234

Kilburn CRJ (1981) Pahoehoe and aa lavas: A discussion and continuation of the model of Peterson and Tilling. J Volcanol Geotherm Res 11:373–382

Kilburn CRJ (1990) Surfaces of aa flow fields on Mount Etna, Sicily: Morphology, rheology, crystallization, and scaling phenomena. In: Lava flows and domes (Fink JH, ed), Springer Verlag, Berlin: 129–156

Longley PA, Batty M (1989) Fractal measurement and line generalization. Comp & Geosci 15:167–183

Lopes RMC, Kilburn CRJ (1990) Emplacement of lava flow fields: Applications of terrestrial studies to Alba Patera, Mars. J Geophys Res 95:14383–14397

Mandelbrot BB (1967) How long is the coast of Britain? Statistical self-similarity and fractional dimension. Science 156:636–638

Mandelbrot BB (1983) The fractal geometry of nature. Freeman, San Francisco, 468 pp

Mueller J-C (1987) Fractal and automated line generalization. Cartographic J 24:27–34

Peterson DW, Tilling RI (1980) Transition of basaltic lava from pahoehoe to aa, Kilauea volcano, Hawaii: field observations and key factors. J Volcanol Geotherm Res 7:271–293

Richardson LF (1961) The problem of contiguity: an appendix to statistics of deadly quarrels. General Systems Yearbook 6:139–187

Rowland SK, Walker GPL (1990) Pahoehoe and aa in Hawaii: volumetric flow rate controls the lava structure. Bull Volcanol 52:615–628

Shaw HR (1969) Rheology of basalt in the melting range. J Petrology 10:510–535

Shaw HR, Swanson DA (1970) Eruption and flow rates of flood basalts. In: Proceedings of the Second Columbia River Basalt Symposium (Gilmour EH, Stradling D, eds), Eastern Washington State College Press, Cheney, 271–299

Shaw HR, Wright TL, Peck DL, Okamura R (1968) The viscosity of basaltic magma: An analysis of field measurements in Makaopuhi lava lake. Am J Sci 266:225–264

Smith AL, Carmichael ISE (1968) Quaternary lavas from the Southern Cascades, Western USA. Contrib Min Petrol 19:212–238

Thorpe RS, Francis PW, O'Callaghan L (1984) Relative roles of source composition, fractional crystallization and crustal contamination in the petrogenesis of Andean volcanic rocks. Philos Trans R Soc London A310:675–692

Turcotte DL (1991) Fractals in geology: What are they and what are they good for? Geol Sci Am Today 1, 1:3–4

Ulrich GE, Bailey NG (1987) Geologic Map of SP Mountain part of San Francisco Volcanic Field, North-Central Arizona. USGS Misc Field Map MF-1956

Wadge G, Lopes RMC (1991) The lobes of lava flows on Earth and Olympus Mons, Mars. Bull Volcanol 54:10–24

Walker GPL (1973) Lengths of lava flows. Philos Trans R Soc London A274:107–118

Editorial responsibility: D. Dzurisin

GEOPHYSICAL RESEARCH LETTERS, VOL. 22, NO. 14, PAGES 1897-1900, JULY 15, 1995

Morphologic identification of Venusian lavas

Barbara C. Bruno[1] and G. Jeffrey Taylor

Planetary Geosciences, Hawaii Institute of Geophysics and Planetology, Honolulu, Hawaii

Abstract. Two independent methods are applied to Venusian lavas. First, fractal properties of 30 lavas are used to identify a'a, pahoehoe and transitional morphologies. Eighteen of these flows are then categorized into these same morphologies based on their radar signal. The techniques produce similar identifications, lending confidence to the fractal identification of those flow margins that could not be studied by the radar technique. Three of these flow margins are of lavas in Mylitta Fluctus, a flood basalt. Our fractal analysis suggests all 3 margins were emplaced as a'a flows, which has implications for the emplacement of large lava plateaux in general.

Introduction

An abundance of evidence indicates that extraterrestrial lavas are generally basaltic; if more silicic flows exist, they are believed to be of limited areal extent (Basaltic Volcanism Study Project, 1981). Specific to Venus, evidence for basaltic composition comes from the Soviet Venera and Vega x-ray fluorescence analyses (Barsukov et al., 1992). The general consensus that Venusian lavas are basaltic has led to speculation on their emplacement. On Earth, high flow rates are associated with channel-fed a'a lavas, whereas lower flow rates tend to produce tube-fed pahoehoe lavas (Peterson and Tilling, 1980) and Venusian lavas would be expected to have similar flow behavior (Head and Wilson, 1986). This work is aimed at better understanding the emplacement of Venusian lavas by identifying a'a and pahoehoe morphologies. Of particular interest is the emplacement of long lavas and flood basalts.

Methodology

Fractal analysis

Our approach is to analyze selected lavas with two independent remote sensing techniques. The first technique, fractal analysis, is described in Bruno et al. (1992, 1994). Briefly, we have found that flow margins of terrestrial basalts are fractal over the range of scales studied (0.125m - 2.4km) provided that they are internally-controlled (i.e., flow margins are shaped by fluid dynamic processes, not by topography). The different styles of emplacement of a'a and pahoehoe flows lead to systematically different flow margin shapes, which can be quantified by the fractal dimension (D). A'a flows generally have lower D ($D \leq 1.09$) than pahoehoe flows ($D \geq 1.13$), and transitional flows tend to have intermediate D.

Using the terrestrial analogy, we perform a fractal analysis on selected Venusian lavas and categorize them into four flow types. Flows that are fractal are interpreted to be internally-controlled basalts. Based on D, these lavas are categorized into a'a, pahoehoe, and transitional morphologies. Non-fractal flows are interpreted to be different from internally-controlled basalts. This category could comprise topographically-controlled basalts (e.g., basalts flowing in pre-existing channels) as well as flows of more evolved compositions.

Radar analysis

Campbell and Campbell (1992) have developed a technique that identifies flows based on their S-band (12.6cm) radar-backscatter signal. A'a flows, having jagged, clinkery surfaces, are systematically rougher than pahoehoe flows at small ($\leq$10's cm) scales, and thus tend to produce a higher backscatter signal at these short wavelengths. Thus, all other factors being equal, a'a flows would appear brighter on radar-backscatter (e.g., Magellan) images than pahoehoe flows.

This technique effectively discriminates between a'a and pahoehoe only when the short-wavelength topography dominates the radar-backscatter return; this occurs at incidence angles (θ) exceeding ~30° (Campbell and Campbell, 1992). At lower θ, the long-wavelength topography significantly contributes to the backscatter signal and this technique cannot be applied. Magellan's Cycle 1 left-looking coverage used $\theta \geq 30°$ at latitudes between 54°N and 34°S; thus lavas located within this band can be categorized as a'a, pahoehoe or transitional. The signal levels corresponding to these flow types vary with θ and therefore latitude.

Comparison between radar and fractal techniques

Our approach is first to analyze only those flows which can be studied by both techniques. We show the two methods produce similar categorizations and thus independently confirm each other. This suggests that the fractal technique is valid and can be applied to identify those flows which cannot be studied with the radar technique. Among those located south of 34°S and hence not suitable for radar analysis are three flow margins of lavas in Mylitta Fluctus, a flow field identified as a flood basalt by Roberts et al. (1992).

Data and Results

We measured the fractal properties of 30 flow margins from Magellan images (75-225m/pix). Flow margins were selected using the criteria of Bruno et al. (1994) and measured using equivalent rod lengths between 140m and 36km. The range of rod lengths used to measure a given margin depends on both the flow margin length and the image scale. We note that there is no gap in scale between the terrestrial and Venusian measurements; in fact, there is more than an order of magnitude overlap in rod lengths. Of these 30 flows, 21 fall within the appropriate latitudinal range for radar analysis. [The remaining 9 are located south of 34°S or north of 54°N.]

Of the 30 flow margins, most (27, or 90%) are fractal over the range of scale measured. Based on the terrestrial analogy, fractal behavior indicates basaltic composition and D can be used to distinguish basaltic flow types (Bruno et al., 1994).

[1]Now at: Department of Earth Sciences, The Open University, Milton Keynes MK7 6AA, England (e-mail: B.C.Bruno@open.ac.uk).

Paper number 95GL01318
0094-8534/95/95GL-01318$03.00

Table 1. Fractal and Radar Analyses of Venusian Flows

Flow number	Flow location (Magellan image)	Fractal Scale (km)	D	R^2	Fractal Interpretation	Radar Interpretation
V1.	W. of Aphrodite Terra (C100N043)	0.6 - 17.9	1.12	.99	trans	phh/trans
V2.	E. of Atla Regio (C100N215)	3.6 - 35.7	1.15	.90	different	
V3.	E. of Atla Regio (C100N215)	2.3 - 28.3	1.09	.90	different	
V4.	E. of Atla Regio (C100N215)	0.5 - 22.5	1.14	.98	phh	trans/phh
V5.	N. of Phoebe Regio (C100N283)	0.6 - 7.1	1.06	.95	a'a	a'a
V6.	N. of Phoebe Regio (C100N283)	0.6 - 7.1	1.07	.90	different	
V7.	N. of Phoebe Regio (C100N283)	0.6 - 9.0	1.06	.97	a'a	a'a
V8.	N. of Phoebe Regio (C100N283)	0.6 - 9.0	1.10	.97	trans	trans/phh
V9.	N. of Phoebe Regio (C100N283)	0.4 - 10.0	1.09	.95	a'a	a'a
V10.	N. of Phoebe Regio (C100N283)	0.5 - 14.0	1.09	.95	a'a	a'a
V11.	E. of Phoebe Regio (C100N317)	0.6 - 17.9	1.13	.98	phh	phh
V12.	N. of Sif Mons (F25N351)	0.3 - 11.1	1.21	.98	phh	phh
V13.	N. of Sif Mons (F25N351)	0.3 - 5.6	1.15	.95	phh	phh
V14.	N. of Sif Mons (F25N351)	1.8 - 17.9	1.20	.96	phh	phh
V15.	N. of Sif Mons (F25N351)	1.4 - 14.2	1.17	.96	phh	phh
V16.	N. of Sif Mons (F25N351)	2.3 - 28.3	1.09	.97	a'a	phh
V17.	N. of Sif Mons (F25N351)	0.3 - 11.1	1.16	.96	phh	phh
V18.	N. of Gula Mons (F25N357)	1.1 - 28.3	1.22	.96	phh	phh
V19.	N. of Gula Mons (F25N357)	0.3 - 8.9	1.16	.98	phh	phh
V20.	N. of Gula Mons (F25N357)	1.8 - 35.7	1.24	.96	phh	phh
V21.	N. of Gula Mons (F25N357)	0.1 - 7.9	1.23	.99	phh	phh
V22.	N. Sedna Planitia (F55N346)	0.3 - 8.9	1.20	.96	phh	
V23.	Mylitta Fluctus (F55S355)	0.4 - 8.9	1.09	.99	a'a	
V24.	Mylitta Fluctus (F55S355)	0.3 - 11.2	1.09	.97	a'a	
V25.	Mylitta Fluctus (F55S355)	0.4 - 5.6	1.04	.98	a'a	
V26.	SE Lavinia Planitia (F50S356)	0.3 - 22.2	1.20	.98	phh	
V27.	SE Lavinia Planitia (F50S356)	0.3 - 7.0	1.21	.97	phh	
V28.	SE Lavinia Planitia (F50S356)	0.3 - 8.9	1.13	.96	phh	
V29.	SE Lavinia Planitia (F50S356)	0.3 - 11.1	1.18	.98	phh	
V30.	SE Lavinia Planitia (F50S356)	0.3 - 11.1	1.18	.98	phh	

Flows are interpreted as a'a ("a'a"), pahoehoe ("phh"), or transitional ("trans") basalts, or different from internally-controlled basalts ("different"). Scale refers to range of rod lengths used in conducting fractal analysis. No radar analysis was performed on flows V22-30 due to their geographic locations, nor on flows V2, V3 and V6, as they are categorized as "different".

Assuming the terrestrial ranges of D also apply to Venusian lavas, we make the following interpretations, as summarized in Table 1: 8 lavas are a'a (D: 1.04-1.09); 17 are pahoehoe (D: 1.13-1.24), and 2 are transitional (D: 1.10-1.12). The three lavas found to be non-fractal are interpreted to be topographically-controlled basalts.

Following Campbell and Campbell (1992), we examine the radar-backscatter signal of the 18 lavas that are both fractal and located between 54°N and 34°S. Based on the level of this signal, we categorize these lavas into a'a (high), transitional (intermediate), and pahoehoe (low) basalts (Fig. 1).

Table 1 compares the radar and fractal categorizations of these 18 flows. Four are identified by both techniques as a'a and 10 are identified by both techniques as pahoehoe. Three flows are identified by the radar technique as having both transitional and pahoehoe morphologies. The corresponding D (1.10, 1.12, and 1.14) are in the transitional or low end of the pahoehoe range. Only one flow (V16) shows an obvious disagreement between the two techniques. This is excellent evidence that Venusian basalts have the same ranges of D as terrestrial basalts, suggesting we can use D to distinguish a'a, pahoehoe and transitional flows on Venus.

Discussion

Radar and fractal techniques

Most (27 of 30) of the flow margins included in this analysis are fractal, indicating a basaltic composition. The three flows classified as different from internally-controlled basalts could represent more evolved lavas, however we favor their interpretation as topographically-controlled basalts.

The fractal dimensions of these lava flow margins indicate both a'a and pahoehoe flows, as well as morphologies transitional between these endmembers. With one exception, this morphologic categorization based on fractal analysis is similar to that based on the radar technique. The one exception is interpreted as a'a by the fractal technique and pahoehoe by the radar technique. In other words, the flow margin appears relatively unconvoluted (a'a-like) yet the surface appears relatively smooth at small scales (pahoehoe-like). This can be explained as a flow emplaced as a'a and subsequently weathered to form a smoother surface. Alternatively, there may be several flows indistinguishable in the Magellan data. A pahoehoe lava having flowed atop a pre-existing a'a lava without obscuring the original flow margins could explain the discrepancy between the two techniques. However, regardless of the exact explanation for this one exception, clearly there is an excellent agreement between the two techniques.

Pahoehoe formation favored on Venus?

We note that the majority of the Venusian flows measured in this study have pahoehoe-like D (Table 1). Similarly, the radar data of the areas studied by Campbell and Campbell (1992) indicate generally smooth (pahoehoe-like) surfaces. Among the explanations put forth by Campbell and Campbell (1992) is that flows are emplaced as a'a but subsequently weather to pahoehoe. This study disfavors that explanation, as weathering of a'a flows would not be expected to create pa-

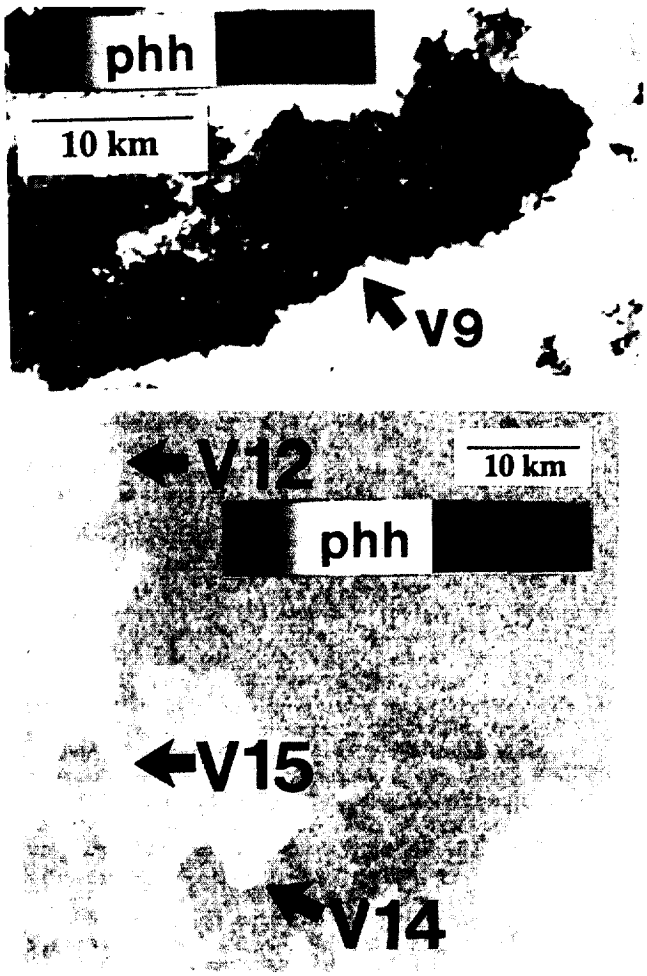

Figure 1. Based on the 12.6cm radar backscatter signal, flows are interpreted as a'a (shown in red), transitional (yellow) and pahoehoe (greyscale). Color bar shows roughness increasing toward the right. Arrows denote flow margins measured with fractal technique; numbers correspond to Table 1. (a) Magellan image C100N283 (resolution 225m/pix). V9 is interpreted as a'a. (b) Magellan image F25N351 (resolution 75m/pix). V12, V14 and V15 are all interpreted as pahoehoe.

hoehoe-like flow margins. Instead, our results suggest flows are emplaced as pahoehoe, likely reflecting modest flow rates.

A priori, it's theoretically difficult to explain why pahoehoe formation would be favored on Venus. In fact, we are not convinced that pahoehoe formation is indeed favored on Venus; this relatively small dataset may well not be representative of the global population of Venusian lavas. However, if more detailed studies using larger databases show that pahoehoe flows are common on Venus -- or on certain volcanoes on Venus -- this has important implications for the sub-volcanic plumbing systems. As summarized by Wilson and Head (1981) and Rowland (1987), an eruption will continue only if magma pressure is sufficient to maintain eruptive conduits, and magma flux is sufficient to replenish heat lost through the cooling of country rocks. Otherwise, the conduit closes and/or the dike freezes, and the eruption stops. The low magma pressures associated with eruptions of pahoehoe lava are insufficient to keep eruptive conduits open; the presence of pahoehoe lavas indicates a pre-established connection between the magma chamber and the planetary surface. Perhaps, the higher shallow crustal temperatures on Venus retard magma

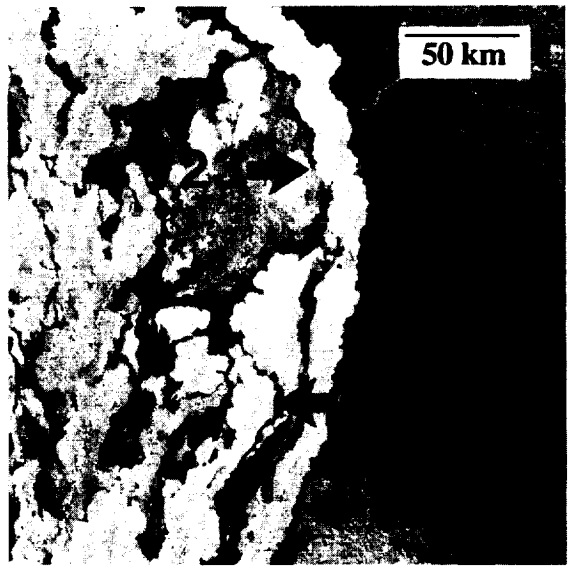

Figure 2. Magellan image F55S355 (resolution 75m/pix) showing long lavas of Mylitta Fluctus flow field.

freezing, thereby keeping dikes fluid longer and allowing them to become mechanically-stable conduits. If the dikes remain fluid for long after the eruption stops, they can be later re-used by subsequent low-magma-flux eruptions.

Long lava flows

As part of this fractal analysis, we studied three flow margins of lavas in Mylitta Fluctus (Fig. 2). In terms of area, volume and thickness, Mylitta Fluctus is comparable to the Columbia River flood basalt province (Table 2). The three measured margins, all found to have a'a-like D, have lengths of ~100-200km, fairly uniform widths of ~20-30km and estimated thicknesses of ~10-30m (Roberts et al., 1992).

There has been much debate on the emplacement of long lavas. Based on terrestrial data, Walker (1973) has argued that long flows are emplaced at high effusion rates. However, Malin's (1980) study of Hawaiian lavas revealed a poor correlation between effusion rate and flow length. Pinkerton and Wilson (1988, 1992) examined the lava flows included in the two datasets and found that Walker's relationship describes cooling-limited channel-fed flows (i.e., Walker's dataset)-- not volume-limited or tube-fed flows. Pinkerton and Wilson's (1992) reanalysis of Malin's data revealed that flows shorter than predicted by Walker's relationship were immature volume-limited flows, whereas flows longer than predicted were tube-fed. As lava tubes significantly inhibit radiative heat losses from the flow surface, flows can travel much greater distances before cooling.

Table 2. Comparison of Flood Basalt Provinces

Flow Field (References)	Area (km^3)	Volume (km^3)	Thickness (m)
Columbia River (Tolan et al., 1989; Reidel et al., 1989)			
Entire Flow Field	$1\text{-}2 \times 10^5$	$1\text{-}2 \times 10^5$	10^3
Individual Flows	$1\text{-}2 \times 10^5$	10^2 - 10^3	~3 - >100
Mylitta Fluctus (Roberts et al., 1992)			
Entire Flow Field	3×10^5	2×10^4	250 - 400 (?)
Individual Flows	$\leq 1 \times 10^5$	$\leq 2 \times 10^4$	10 - 30 (?)

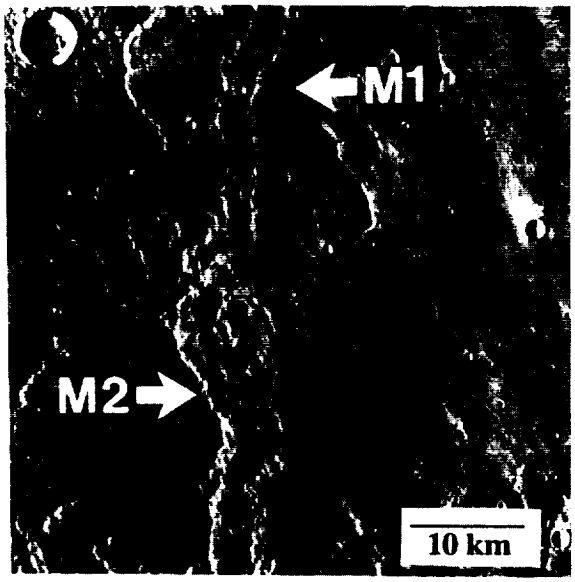

Figure 3. Photomosaic of Viking Orbiter frames 651A07-12 (resolution 52m/pix), showing long lavas in Elysium Planitia, Mars. (After Mouginis-Mark, 1985.)

Thus two theories are offered to explain the long lavas of Mylitta Fluctus (and other flood basalts): (1) channel-fed a'a lavas associated with unusually high effusion rates or (2) tube-fed pahoehoe lavas, generated by modest emplacement rates over unusually long eruption durations. Fractal analysis of the three margins studied revealed a'a-like D, favoring the former explanation and suggesting that at least this episode of Mylitta Fluctus was emplaced at high flow rates.

For comparison, we also performed a fractal analysis on morphologically-similar lavas in Elysium Planitia, Mars (Fig. 3). Like the Mylitta Fluctus lavas, these flows are long (~100-200km), narrow (~10km), and have fairly uniform widths (Mouginis-Mark, 1992). Recent photoclinometric measurements yielded average flow thicknesses of ~30-50km (M. Tatsumura, University of Hawaii, unpublished data, 1994). Fractal dimensions of these flow margins were 1.04 and 1.08, again indicating a'a morphologies (Bruno, 1994).

These a'a-like D indicate that these long lava flows are emplaced in open channels, probably at high flow rates. Even if an underground tube system is present, as suggested by Mouginis-Mark (1992), their emplacement is vastly different from pahoehoe emplacement. The low D indicate the absence of the branching tube systems that characterize terrestrial pahoehoe flow fields and result in a convoluted flow margin (Bruno et al., 1994; Taylor, 1992). Instead, most of the lava appears to be transported along one main pathway, resulting in a flow of uniform width with a linear flow margin.

Conclusions

Most (27 of 30) of the Venusian lavas included in this study are fractal, indicating a basaltic composition, with fractal dimensions similar to the terrestrial range. Combining the terrestrial and Venusian data, the fractal nature of lava flow outlines holds over five orders of magnitude in scale: from 10cm to 36km. Using fractal dimension, we have remotely identified Venusian flows as a'a, pahoehoe and transitional basalts, and this identification has been independently confirmed by a radar technique. Such flow type identification can lead to a better understanding of planetary eruption rates and eruption styles. Our fractal analysis of Mylitta Fluctus suggests that this flood basalt province has been emplaced as a'a flows.

Acknowledgments. This research was funded by National Aeronautics and Space Administration (NASA) grants NGT 50930 (Graduate Student Researchers Program) and NAGW 3684 (Planetary Geology and Geophysics Program). Useful comments were provided by Lionel Wilson and an anonymous reviewer. We thank Scott Rowland and Michelle Tatsumura for helpful discussions and Harold Garbeil for software support. Many thanks go to Bruce Campbell for sharing his computer programs. This is SOEST Contribution No. 3863 and Planetary Geosciences Paper No. 803.

References

Barsukov, V. L., A. T. Basilevsky, V. P. Volkov, and V. N. Zharkov (Eds.), *Venus geology, geochemistry and geophysics*, 420 pp., University of Arizona Press, Tucson, 1992.

Basaltic Volcanism Study Project, *Basaltic Volcanism on the Terrestrial Planets*, 1286 pp., Pergamon Press, Inc., New York, 1981.

Bruno, B. C., Lava flow dynamics: Clues from fractal analysis, Ph.D. dissertation, 247 pp., Univ. of Hawaii, Honolulu, December 1994.

Bruno, B. C., G. J. Taylor, S. K. Rowland, P. G. Lucey, and S. Self, Lava flows are fractals, *Geophys. Res. Lett., 19*, 305-308, 1992.

Bruno, B. C., G. J. Taylor, S. K. Rowland, and S. M. Baloga, Quantifying the effect of rheology on lava-flow margins using fractal geometry, *Bull. Volcanol., 56*, 193-206, 1994.

Campbell, B. A., and D. B. Campbell, Analysis of volcanic surface morphology on Venus from comparison of Arecibo, Magellan and terrestrial airborne radar data, *J. Geophys. Res., 97*, 16293-16314, 1992.

Head, J. W., and L. Wilson, Volcanic processes and landforms on Venus: Theory, predictions and observations, *J. Geophys. Res., 91*, 9407-9446, 1986.

Malin, M. C., Lengths of Hawaiian lava flows, *Geol., 8*, 306-308, 1980.

Mouginis-Mark, P. J., Emplacement of long lava flows at Elysium Mons, Mars (abstract), *Lunar Planet. Sci., XXIII*, 939-940, 1992.

Peterson, D. W., and R. I. Tilling, Transition of basaltic lava from pahoehoe to aa, Kilauea volcano, Hawaii: field observations and key factors, *J. Volc. Geotherm. Res., 7*, 271-293, 1980.

Pinkerton, H., and L. Wilson, The lengths of lava flows (abstract), *Lunar Planet. Sci., XIX*, 937-938, 1988.

Pinkerton, H., and L. Wilson, The dynamics of channel-fed lava flows (abstract), *Lunar Planet. Sci., XXIII*, 1083-1084, 1992.

Reidel, S. P., T. L. Tolan, P. R. Hooper, M. H. Beeson, K. R. Fecht, R. D. Bentley and J. L. Anderson, The Grand Ronde Basalt, Columbia River Basalt Group: Stratigraphic descriptions and correlations in Washington, Oregon and Idaho, in *Volcanism and Tectonism in the Columbia River Flood Basalt Province*, edited by S. P. Reidel and P. R. Hooper, Geol. Soc. Amer. Spec. Pap. 239, 21-53, 1989.

Roberts, K. M., J. E. Guest, J. W. Head, and M. G. Lancaster, Mylitta Fluctus, Venus: Rift-related, centralized volcanism and the emplacement of large-volume flow units, *J. Geophys. Res., 97*, 15991-16015, 1992.

Rowland, S. K., The flow character of Hawaiian basalt lavas, Ph.D. dissertation, 118 pp., Univ. of Hawaii, Honolulu, August 1987.

Taylor, G. J., Fractal properties of lava tube systems (abstract), *Eos Trans. AGU, 73*, 648, 1992.

Tolan, T. L., S. P. Reidel, M. H. Beeson, J. L. Anderson, K. R. Fecht and D. A. Swanson, Revisions to estimates of the areal extent and volume of the Columbia River Basalt Group, in *Volcanism and Tectonism in the Columbia River Flood Basalt Province*, edited by S. P. Reidel and P. R. Hooper, Geol. Soc. Amer. Spec. Pap. 239, 1-20, 1989.

Walker, G. P. L., Lengths of lava flows, *Phil. Trans. R. Soc. Lond., A274*, 107-118, 1973.

Wilson, L., and J. W. Head, Ascent and eruption of basaltic magma on the Earth and Moon, *J. Geophys. Res., 86*, 2971-3001, 1981.

B. Bruno and G. Taylor, Planetary Geosciences, Hawaii Institute of Geophysics and Planetology, Honolulu, HI 96822.

(Received January 11, 1995; accepted March 17, 1995.)

JOURNAL OF GEOPHYSICAL RESEARCH, VOL. 101, NO. B5, PAGES 11,565–11,577, MAY 10, 1996

Modeling gravity-driven flows on an inclined plane

Barbara C. Bruno

Department of Earth Sciences, The Open University, Milton Keynes, England

Stephen M. Baloga

Proxemy Research Incorportated, Laytonsville, Maryland

G. Jeffrey Taylor

Hawaii Institute of Geophysics and Planetology, University of Hawaii at Manoa, Honolulu, Hawaii

Abstract. We develop an exact analytic solution for unconfined flows having an assumed rheology advancing on an inclined plane. We consider the time-dependent flow movement to be driven by gravitational transport and hydrostatic pressure. We examine how these two forces drive flow movement in the downstream and cross-stream directions by adopting a volume conservation approach. Simplifying assumptions reduce the governing equation to the dimensionless form $\partial/\partial x(\alpha h^m) = \partial/\partial y(\alpha h^m \partial h/\partial y)$, where x and y are the downstream and cross-stream directions, respectively; h is the flow depth; and $\alpha = \alpha(x)$ and m are prescribed by the rheology of the fluid. We solve this equation analytically for flows of arbitrary m and α using a similarity transformation. This method involves transforming variables and reducing the governing equation to a nonlinear ordinary differential equation. Our solution determines how flow depth and width change with distance from the source of the flow for different α and m based on known or assumed initial parameters. Consequently, from the traditional geometric dimensions of the deposits, these rheological parameters can be inferred. We have applied the model to basaltic lava flows and found m values typically between 1 and 2. This contrasts with Newtonian fluids, for which m=3. The model of $\alpha(x)$ corresponding to constant viscosity approximates the field data of pahoehoe toes (<5 meters in length), whereas models of $\alpha(x)$ corresponding to linearly increasing and exponentially increasing viscosities better approximate the remote sensing data of longer flows (several kilometers in length).

Introduction

Bruno et al. [1992, 1994] developed a technique to glean information regarding flow emplacement and rheology from the fractal properties of lava flow margins. We found that as frozen snapshots of the final moments of flow, plan view shapes hold important information regarding lava flow dynamics and rheology. In this work, we again exploit the final shape of a lava flow as a source of rheological information, using an altogether different method. We model downstream changes in flow depth and width for flows of different rheological characteristics, and then apply this model "backward" to infer or constrain these rheological characteristics given depth and width profiles. We note that this model can also be applied to other types of unconfined geologic deposits, such as volcanic lahars and mud flows.

A critical assumption of the formulation of the problem is that the volumetric flow rate in the downstream direction represents a conserved quantity. The conservation of volume for an unconfined flow of depth $h = h(x, y, t)$ on an inclined plane is described by

$$\frac{\partial h}{\partial t} + \vec{\nabla}\vec{q} = 0 \tag{1a}$$

where

$$\vec{\nabla} = \frac{\partial}{\partial x}\vec{i} + \frac{\partial}{\partial y}\vec{j} \tag{1b}$$

and where t is time; q is the volumetric flow rate per unit width; and x and y are the spatial coordinates in the downstream and cross-stream directions, respectively. (All mathematical symbols are summarized in the notation section.) Equation (1a) is a form of the first-order conservation equation relating flow of a given variable (i.e., h) to its time rate of change. Solutions to these equations are called kinematic waves [e.g., *Lighthill and Whitham*, 1955; *Baloga*, 1987]. Applying kinematic wave theory to volcanic lahars and considering only the downstream (x) direction, *Weir* [1982] considered solutions to (1a) of the form

$$q = bf(\theta)h^m \tag{2}$$

where b and m are constants and $f(\theta)$ is some function of surface slope. As noted by *Weir* [1982], many different types of transport processes have been modeled with a flow rate of the form shown in (2) featuring a power law relationship between flow rate (q) and flow depth (h), a spatially dependent prefactor β (which in (2) depends on a

Paper number 96JB00178.
0148-0227/96/96JB-00178$09.00

constant b and the surface slope θ) and a positive constant m. The empirically determined m values of 3/2 and 5/3 give the Chezy and Manning laws, respectively, for rivers with β dependent on the square root of the slope. The Shamov law is given by m=7/6 with β independent of slope, whereas the Sribniy law is given by m=5/3 with β dependent on the fourth root of slope. Both the Shamov and Sribniy laws have been used to describe transport of mud flows [*Gol'din and Lyubashevskiy*, 1966]. In quantifying the risk from volcanic lahars, *Weir* [1982] obtained m values in the range 1.2-2.0 with a β dependence on the underlying slope similar to that of empirical river laws. Other diverse applications based on a flow rate of the form of (2) include rainfall runoff [*Sherman*, 1978], channel flow with infiltration [*Sherman*, 1981], laminar flow of glaciers [*Paterson*, 1969, chapter 6], surface irrigation [*Sherman and Singh*, 1978], and dam bursting [*Hunt*, 1982]; see *Weir* [1982, 1983] for a thorough review of the literature. The classic treatment of such flow rate forms derives from the problem of river flooding [*Lighthill and Whitham*, 1955] with other notable early papers addressing the response of glaciers to various environmental factors [e.g., *Nye*, 1960, 1963].

In this work, we explore the relevance of a flow rate of the form of (2) in describing transport of lava flows of arbitrary rheology. Our approach is to generalize the volumetric flow rate per unit width of Newtonian fluids given by

$$\vec{q} = -\frac{g}{3\nu}\cos\theta h^3 \vec{\nabla} h + \frac{g}{3\nu}\sin\theta h^3 \vec{i} \tag{3}$$

to include *Weir*'s [1982] relation (equation (2)). Thus we adopt the generalized flow rate

$$\vec{q} = -\alpha g\cos\theta h^m \vec{\nabla} h + \alpha g\sin\theta h^m \vec{i} \tag{4}$$

where $\alpha=\alpha(x)$ and m, a positive constant, are prescribed by the rheology of the fluid. Our approach is to solve the volume conservation equation (equation (1a)) using the flow rate given in (4) and to compare the theoretical solution with data. If the solution describes the data, we shall conclude the assumed flow rate is a reasonable model for lava flows; otherwise, we will conclude that the assumed flow rate is not appropriate. We note that (4) does not account for instabilities (e.g., due to surface tension); the possible development of instabilities in viscous fluids has been addressed in the literature [*Huppert*, 1982a, b; *Lister*, 1992].

Equation (4) incorporates *Weir*'s [1982] power law dependence on flow depth and an arbitrary spatially dependent change in the rheological parameter α. We note that this assumed power law relationship is unrelated to the power law relationship between shear stress and strain rate (i.e., "power law rheology") that characterizes certain fluids. Like (2), equation (4) expresses the influence of gravity in the downstream (x) direction and the influence of hydrostatic pressure according to the gradient of the depth of the flow. For Newtonian fluids of constant viscosity (m=3 and $\alpha=1/3\nu$, where ν is kinematic viscosity), equation (4) reduces to (2). *Smith* [1973] found an analytical solution for this special case [see also *Lister*, 1992]. For non-Newtonian flows, the parameter m may be greater or less than 3 and can be empirically determined by comparing our solution to (4) with flow shape. If, for example, the associated flow depth for a non-Newtonian fluid is less than the Newtonian equivalent for a given flow rate, then it follows that $m > 3$.

For flows of nonconstant viscosity, the parameter α is free to vary spatially. However, this spatial dependence is permitted only in the downstream direction; any cross-stream variations in viscosity are assumed to be small in comparison with changes in the downstream direction. Like m, $\alpha(0)$ is a positive constant.

Smith [1973] showed that substituting the flow rate for a Newtonian fluid (equation (2)) into the volume conservation law (equation (1a)) generates a differential equation having the form of the nonlinear diffusion equation under certain restrictions and simplifications with free boundaries on the surface of the flow. Obtaining this differential equation requires that gravity is the predominant influence on the downstream motion (i.e., the influence of the hydrostatic pressure gradient in the downstream direction is relatively small), while the concomitant lateral expansion of the flow is due solely to hydrostatic pressure. In the steady state, *Smith* [1973] found a remarkable similarity solution that matches the free-boundary condition for the lateral expansion of the flow as a function of distance from the source.

In this paper, we generalize the volumetric flow rate used by *Smith* [1973] to embrace *Weir*'s [1982] relation and an arbitrary spatially dependent change in the flow viscosity. To solve the resulting nonlinear diffusion equation for volume conservation, we show that there exists a transformation of the differential equation into the original *Smith* [1973] form and obtain corresponding solutions for different types of rheologies. As required by the case of a Newtonian fluid of constant viscosity [*Smith*, 1973], the generalized case requires both that gravity is the predominant influence on the downstream motion and the accompanying widening of the flow downstream is due solely to hydrostatic pressure.

Steady State Similarity Solution

The solution described in this section applies to the steady state, i.e.,

$$\vec{\nabla}\vec{q} = 0. \tag{5}$$

The steady state (or time-independent) solution is presumably the asymptotic form of physically reasonable time-dependent solutions. At the source of the flow, we have the boundary conditions

$$h\,(x = 0, y = 0) = h_0 \tag{6a}$$

$$h\,(x = 0, y = \pm w_0) = 0 \tag{6b}$$

where h_0 and w_0 are prescribed positive constants which represent the depth and half width of the flow, respectively, at the source. Because the flow margin is a free boundary and can expand according to the local dynamics, we must also find the function $w=w(x,t)$ such that for all $t \geq 0$,

$$h\,(x\,, y = \pm w) = 0 \tag{6c}$$

that is, the flow has a finite width. We do not require that a comparable boundary condition be satisfied in the downstream direction, thus allowing the flow to have infinite length.

To obtain an exact analytic solution in the steady state, we convert the steady state partial differential equation and supplementary conditions to dimensionless form using the following substitutions:

$$h = h_0 h^* \tag{7a}$$

$$x = L x^* \tag{7b}$$

$$y = w_0 y^* \tag{7c}$$

$$w = w_0 w^* \tag{7d}$$

$$\alpha = \alpha_0 \alpha^* \tag{7e}$$

where asterisked parameters are dimensionless and the downstream length scale (L) is yet to be determined. Unlike the other scaling factors (h_0, w_0 and α_0), the parameter L does not represent a condition at the source nor is it constrained by flow dimensions; it is a free parameter.

Combining (4), (5), and (7) results in the dimensionless partial differential equation

$$\frac{\partial}{\partial y^*}\left(\alpha^* h^{*m}\frac{\partial h^*}{\partial y^*}\right)+\left(\frac{w_0}{L}\right)^2\frac{\partial}{\partial x^*}\left(\alpha^* h^{*m}\frac{\partial h^*}{\partial x^*}\right) = \left(\frac{\sin\theta {w_0}^2}{\cos\theta L h_0}\right)\frac{\partial}{\partial x^*}\left(\alpha^* h^{*m}\right) \tag{8a}$$

or, dropping asterisks to simplify notation (but remembering all terms are dimensionless),

$$\frac{\partial}{\partial y}\left(\alpha h^m\frac{\partial h}{\partial y}\right)+\left(\frac{w_0}{L}\right)^2\frac{\partial}{\partial x}\left(\alpha h^m\frac{\partial h}{\partial x}\right)=\left(\frac{\sin\theta {w_0}^2}{\cos\theta L h_0}\right)\frac{\partial}{\partial x}\left(\alpha h^m\right). \tag{8b}$$

The corresponding dimensionless form of the supplementary conditions is given by

$$h\,(x=0,\,y=0)=1 \tag{9a}$$

$$h\,(x=0,\,y=\pm 1)=0 \tag{9b}$$

$$h\,(x,\,y=\pm w(x))=0 \tag{9c}$$

$$\partial h/\partial y\,(x,\,y=0)=0 \tag{9d}$$

$$w(0)=1 \tag{9e}$$

$$\alpha(0)=1. \tag{9f}$$

In the interest of simplifying (8b), we define the length scale

$$L=\frac{w_0^2}{h_0}\tan\theta. \tag{10a}$$

Furthermore, we require that the influence of the hydrostatic pressure in the downstream direction is small compared to the direct gravitational transport of fluid elements and the cross-stream influence of hydrostatic pressure such that

$$\left(\frac{w_0}{L}\right)^2\frac{\partial}{\partial x}\left(\alpha h^m\frac{\partial h}{\partial x}\right)\ll 1 \tag{10b}$$

and can therefore be disregarded. The partial differential equation (8b) can then be written in the form

$$\frac{\partial}{\partial x}\left(\alpha h^m\right)=\frac{\partial}{\partial y}\left(\alpha h^m\frac{\partial h}{\partial y}\right). \tag{11}$$

When the geometric considerations for a flow indicate that (10b) is satisfied, solutions to (11) describe how flow depth changes, both downstream and laterally. We will then be able to solve for the unknown function $w=w(x)$, which describes how flow width changes downstream.

Smith [1973] solved (11) analytically for a Newtonian fluid (i.e., $m=3$ and $\alpha(x)=1/3\nu$, where ν is kinematic viscosity) with a constant viscosity using the method of similarity transformation. Our approach requires transformation of (11) to the form obtained by Smith, but our subsequent analysis highlights some important differences for the dynamics of the problem.

We begin our approach by transforming away the dependence on the arbitrary function $\alpha(x)$ in the governing (11). This function characterizes the spatially dependent resistance to flow caused by viscosity, surface friction, and any other forces. Here, we rid our equation of $\alpha(x)$, leaving a transformed equation that can be more readily solved by similarity methods, even though the arbitrary function remains embedded in the dependent and independent variables. Instead of a differential equation for h, we transform the partial differential equation to one that applies to a related variable ξ defined by

$$h(x,y)=\alpha(x)^{-1/m}\xi(x,y). \tag{12}$$

Instead of the independent variable x, we use a related variable z:

$$z=\int_0^x\frac{dx'}{\alpha(x')^{1/m}}. \tag{13}$$

With these new variables, (11) becomes

$$\frac{\partial}{\partial z}\left(\xi^m\right)=\frac{\partial}{\partial y}\left(\xi^m\frac{\partial\xi}{\partial y}\right). \tag{14a}$$

Explicitly differentiating (14a) yields the equivalent expression

$$\frac{\partial\xi}{\partial z}=\frac{\xi}{m}\frac{\partial^2\xi}{\partial y^2}+\left(\frac{\partial\xi}{\partial y}\right)^2. \tag{14b}$$

Equation (14b) is a partial differential equation with one dependent variable (ξ) and two independent variables (y,z). It is a transformed version of (11) which also has one dependent variable (h) and two independent variables (x,y). We now apply a similarity construct for the purpose of transforming (14b) into an ordinary differential equation with one dependent variable (G) and one independent variable (η). Following *Smith* [1973], we introduce the similarity construct

$$\xi(\eta,z)=(1+az)^r\,G(\eta) \tag{15}$$

with

$$\eta=y(1+az)^q \tag{16}$$

where a, r, and q are positive constants to be determined.

This construct will constitute a similarity solution provided (1) the constants a, r, and q can be determined; (2) the partial differential equation (14b) reduces to an ordinary differential equation; and (3) the resulting ordinary differential equation has a solution that satisfies boundary conditions corresponding to those appearing in (9).

With the transformations shown in (15) and (16), the supplementary conditions shown in (9) translate to

$$G(0) = 1 \tag{17a}$$

$$G'(0) = 0 \tag{17b}$$

$$G(\pm 1) = 0 \tag{17c}$$

The reader may check, by explicitly differentiating (15), that

$$\frac{\partial \xi}{\partial z} = a(1+az)^{r-1}\left[rG + q\eta G'\right] \tag{18a}$$

$$\frac{\partial \xi}{\partial y} = (1+az)^{r+q} G' \tag{18b}$$

$$\frac{\partial^2 \xi}{\partial^2 y} = (1+az)^{r+2q} G'' \tag{18c}$$

Substituting the expressions of (18) into (14b) yields

$$a(1+az)^{r-1}\left[rG + q\eta G'\right] = (1+az)^{2r+2q}\left[\frac{GG''}{m} + G'^2\right]. \tag{19}$$

Note that the factor $(1+az)$ appears on each side of (19) with different exponents. By definition, similarity transformations are absolutely invariant; they necessarily preserve power relationships. Thus the constants r and q are required to satisfy

$$2r + 2q = r - 1. \tag{20}$$

The governing equation becomes

$$\left[\frac{GG''}{m} + G'^2\right] - a\left[rG + q\eta G'\right] = 0. \tag{21}$$

and we look for a solution of the form

$$G = c_1 + c_2\eta + c_3\eta^2 \tag{22}$$

noting that there may be other solutions to (21) that are not of the form of (22). From the boundary conditions listed in (17), the solution to (22) is determined to be

$$G = 1 - \eta^2. \tag{23}$$

The reader may check that the solution shown in (23) also satisfies (17b), as required. Substituting (23) into (21),

$$\frac{-2}{m}(1-\eta^2) + 4\eta^2 - a\left(r + \eta^2\right)\left(-r - 2q\right) = 0 \tag{24a}$$

and, from (20),

$$\frac{-2}{m}(1-\eta^2) + 4\eta^2 - a\left[r + \eta^2\right] = 0. \tag{24b}$$

We now wish to solve for the three unknown constants (a, r, q). All three constants appear in the similarity construct and can be related explicitly to m, the only parameter of the transformed differential equation (11). By equating coefficients of powers of η in (24b), we obtain two conditions for the constants r and a, required for a solution of the governing equation (21):

Equating coefficients of η^2

$$\frac{2}{m} + 4 - a = 0. \tag{25a}$$

Equating coefficients of η^0

$$\frac{-2}{m} - ar = 0. \tag{25b}$$

With (20), we have three equations for three unknowns (a, r, q). The result is

$$a = 2(1+2m)/m \tag{26a}$$

$$r = -1/(1+2m) \tag{26b}$$

$$q = -m/(1+2m). \tag{26c}$$

This completes the solution of the problem in the sense that all constants required by the similarity construct are given in terms of the parameter m, and once some form of $\alpha(x)$ has been chosen, (13), (15), (16), and (23) can be used to relate the integral in (12) back to the h variable. The solution is

$$h(x,y) = \alpha^{-1/m}\left(1 + a\int_0^x \frac{dx'}{\alpha^{1/m}}\right)^r\left[1 - y^2\left(1 + a\int_0^x \frac{dx'}{\alpha^{1/m}}\right)^{2q}\right] \tag{27}$$

where a, r, and q are given in terms of m in (26) and $\alpha=\alpha(x)$ is arbitrary. We note that for Newtonian fluids (m=3), our solution reduces to *Smith*'s [1973] solution, with a=14/3, r=-1/7 and q=-3/7.

Recall that the variables in (27) are dimensionless; they were nondimensionalized according to the transformations of (7). Here, we undo those transformations, arriving at

$$\left(1 + a\alpha_0^{1/m}\int_0^{x/L} \frac{dx'}{\alpha^{1/m}}\right)^r\left[1 - \frac{y^2}{w_0^2}\left(1 + a\alpha_0^{1/m}\int_0^{x/L} \frac{dx'}{\alpha^{1/m}}\right)^{2q}\right]. \tag{28}$$

The explicit form of $w(x)$ naturally follows from (6c) and (28). At the flow margin (i.e., $y=\pm w$),

$$1 - \frac{y^2}{w_0^2}\left(1 + a\alpha_0^{1/m}\int_0^{x/L} \frac{dx'}{\alpha^{1/m}}\right)^{2q} = 0 \tag{29a}$$

therefore

$$w = w_0\left(1 + a\alpha_0^{1/m}\int_0^{x/L} \frac{dx'}{\alpha^{1/m}}\right)^{-q}. \tag{29b}$$

Effect of Rheology on the Steady State Similarity Solution

The steady state similarity solution $h(x,y)$ (equation (28)) has a rheological dependence; both $\alpha(x)$ and m are prescribed

by the rheology of the fluid. We note, with the conditions given in (6), that regardless of the values of $\alpha(x)$ and m, (28) reduces to

$$h(0,y)=h_0\left(1-y^2/w_0^2\right). \tag{30}$$

The similarity method produces a physically realistic boundary condition: equation (30) indicates a parabolic cross section at the vent. The downstream evolution of this parabolic form, however, varies with the rheological characteristics. Here, we show the effect of various values of $\alpha(x)$ and m on the form of $h(x,y)$ both in cross-sectional and longitudinal profiles. In the following section, we compare the resulting profiles with data obtained from field and photographic measurements.

Models for $\alpha(x)$

During surface flow, a lava (or other geologic material) often experiences a change in resistance to flow. This could be due to changes in the fluid's properties (e.g., a downstream increase in viscosity in a lava due to cooling or crystallization) and/or changes in the underlying topography (e.g., changes in the slope or roughness of the underlying flow bed). Determining the nature of these processes and their effect on $\alpha(x)$ requires either empirical data from specific applications or an independent physical law, such as a cooling-induced viscosity or crystallinity change. In the absence of such information, we consider three end-member models to approximate the form of changes in $\alpha(x)$ with distance from the source of the flow. These choices of $\alpha(x)$ are arbitrary, but based on our knowledge that at least for Newtonian flows, $\alpha(x)$ is inversely related to viscosity. Here, we assume that $\alpha(x)$ is inversely related to viscosity in the general, non-Newtonian case and construct three models for $\alpha(x)$ correspond to constant, linearly increasing and exponentially increasing viscosity:

Constant $$\alpha(x)=\alpha_0 \tag{31a}$$

Linear $$\alpha(x)=\alpha_0/(1+x/L_\alpha) \tag{31b}$$

Exponential $$\alpha(x)=\alpha_0 e^{-x/L_\alpha} \tag{31c}$$

where $\alpha_0=\alpha(0)$ and L_α is a constant scale factor. For laminar flow of Newtonian fluids, $\alpha_0=1/3v_0$, where v_0 is the viscosity at the source of the flow. Equation (31a) precludes any downstream changes in viscosity, thus requiring α to remain constant. Equations (31b) and (31c) allow for downstream viscosity changes. In formulating these two equations, we assumed viscosity increases downstream. For many geological materials (including silicate lava flows), this is consistent with observations that cooling and crystallization induce viscosity increases. However, this is not always the case; some materials (e.g., sulfur) show a decrease in viscosity during cooling in certain temperature ranges, and the reader is hereby cautioned. The rate at which viscosity increases (and $\alpha(x)$ decreases) in (31b) and (31c) is related to some scale factor L_α, which is generally controlled by physical processes (e.g., crystallization) and may be unrelated to the length scale L defined in (7b).

Effect of Rheology on the Solution

In this section we substitute the expressions for $\alpha(x)$ given in (31) into our solution for flow depth (equation (28)) and half width (equation (29b)) along with selected m values to determine the dependence of our solution on these rheological parameters. We note that the purpose of these calculations is to examine flow behavior for various flow regimes and not to model a realistic flow. Also required by these equations are flow depth and half width at the source (h_0 and w_0) and surface slope θ. Arbitrarily chosen sample values used in this analysis are given here: w_0=10 m, h_0=1 m and θ=5.7°. Substituting these parameters into (28) and (29b) allows us to construct depth and width profiles, respectively, for choices of $\alpha(x)$ and m and thus to determine the effect of these rheological parameters on our solution. Longitudinal depth and width profiles are shown for selected

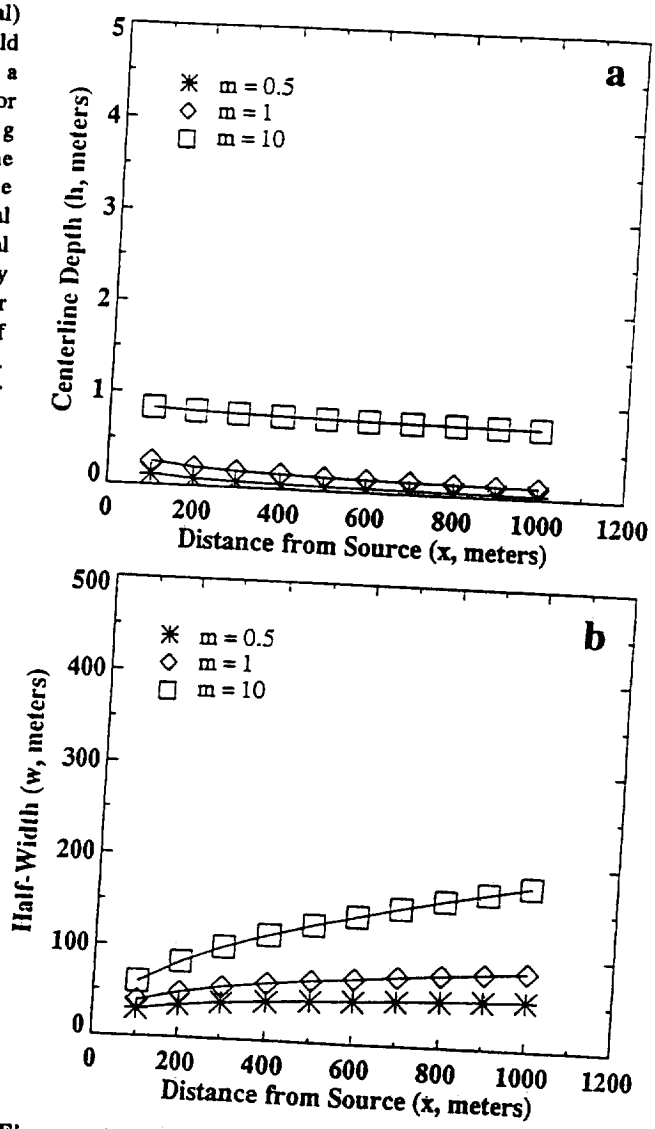

Figure 1. Theoretical longitudinal profiles of (a) centerline flow depth and (b) flow half width as a function of distance from source, based on constant viscosity and assumed initial parameters. These profiles correspond to m=0.5, m=1, and m=10. All flows (regardless of m values) widen downstream, accompanied by modest thinning. Higher m values correspond to wider, thicker flows having higher aspect ratios.

m values (0.5, 1, and 10) for constant (Figure 1), linearly increasing (Figure 2) and exponentially increasing viscosity (Figure 3).

For constant α, all flows (regardless of m values) widen downstream (Figure 1). Flow depth remains relatively constant, showing a slight downstream thinning. Higher m values correlate with wider, thicker flows of higher aspect ratios (h/w). Near the source, the flow has the highest aspect ratio; cross-sectional profiles become progressively thinner and wider downstream. All flows show convex longitudinal depth (h versus x) profiles (Figure 1a) and concave longitudinal width (w versus x) profiles (Figure 1b).

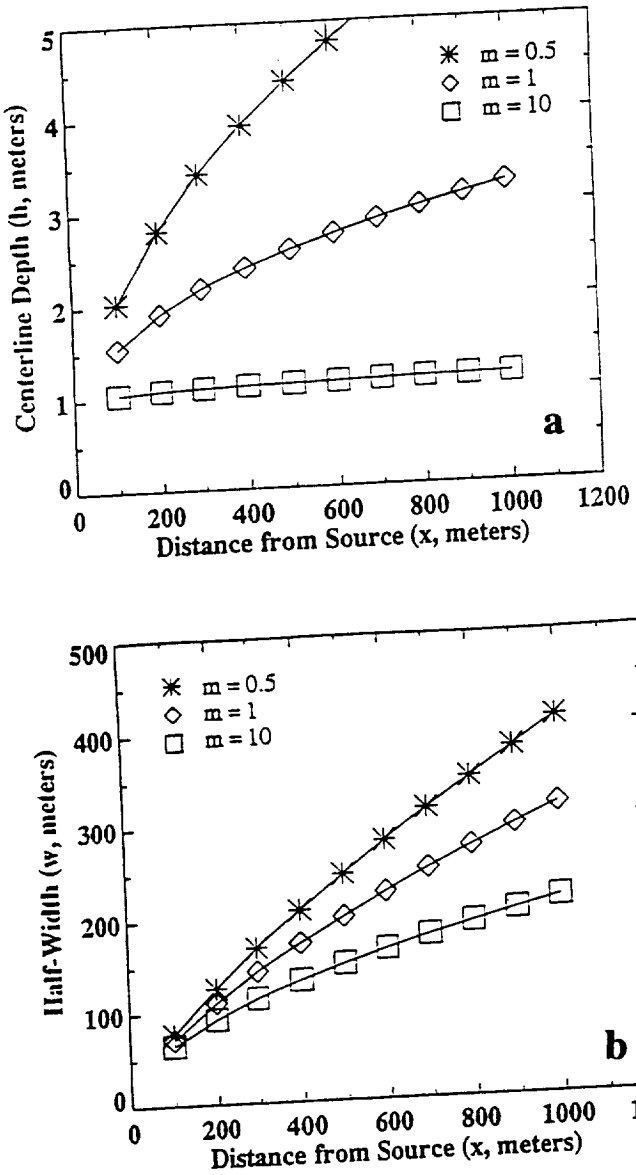

Figure 2. Theoretical longitudinal profiles of (a) centerline flow depth and (b) flow half width as a function of distance from source, based on linearly increasing viscosity and assumed initial parameters including L_α=10 (100-fold viscosity increase). These profiles correspond to m=0.5, m=1, and m=10. All flows (regardless of m values) thicken and widen downstream. Lower m values generally correlate with wider, thicker flows having higher aspect ratios.

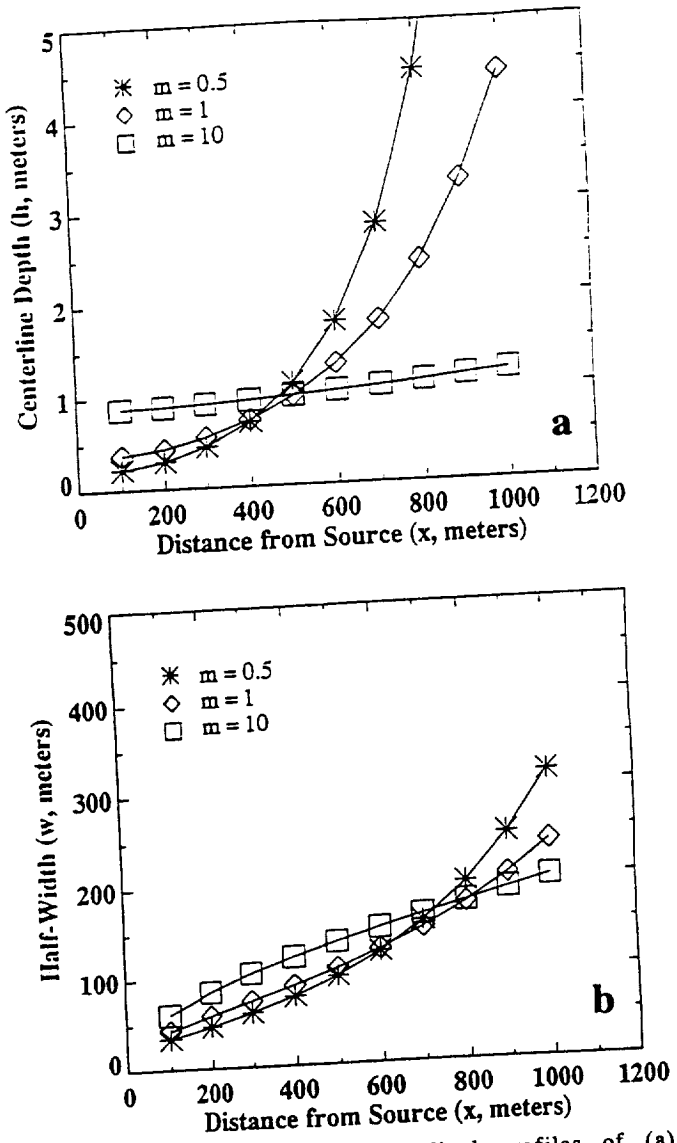

Figure 3. Theoretical longitudinal profiles of (a) centerline flow depth and (b) flow half width as a function of distance from source, based on exponentially increasing viscosity, and assumed initial parameters including L_α=215 (100-fold viscosity increase). These profiles correspond to m=0.5, m=1, and m=10. All flows (regardless of m values) thicken and widen downstream, but flows characterized by low m values show only modest widening and thickening over the distance shown (1 km).

For linear α (i.e., linearly increasing viscosity), flows tend to thicken and widen downstream. Unlike the case of constant α, lower m values generally correlate with wider, thicker flows having higher aspect ratios (Figure 2). Both the longitudinal depth (Figure 2a) and width (Figure 2b) profiles are concave. Compared with the case of constant α, these flows are wider and thicker, with the differences becoming more pronounced downstream, that is, as the differences in $\alpha(x)$ become more significant.

There is a strong dependence on the choice of scaling factor L_α. For sufficiently large values of L_α, downstream increases in $\alpha(x)$ are negligible, approximating constant viscosity. Thus the flow would exhibit a near-constant, slowly decreasing depth in a convex longitudinal depth

profile. Choosing sufficiently small L_α, the downstream longitudinal profile would show continuous thickening, most noticeably for low m values. Figure 2 is based on L_α=10 in (31b), which corresponds to a downstream viscosity increase of 100-fold over the first kilometer. This downstream viscosity increase is realistic for basaltic lavas, as discussed below.

For exponential α (i.e., exponentially increasing viscosity), flows tend to thicken and widen downstream. Like Figure 2, Figure 3 corresponds to a viscosity increase of 2 orders of magnitude over the first kilometer. This corresponds to L_α=215 in (31c). Flow depth (Figure 3a) and width (Figure 3b) each increase exponentially downstream. Longitudinal depth profiles are convex, whereas the width profiles may show a change in concavity from concave near the source to convex farther downstream. Flows characterized by low m values show only modest widening and thickening near the source; however, farther downstream, these flows eventually become thicker and wider than those characterized by higher m values. Again, there is a strong dependence on the choice of L_α. Choosing a smaller value for L_α would result in significantly wider and thicker longitudinal profiles.

Our model predicts that flows characterized by downstream viscosity increases (either linear or exponential) are typically thicker and wider than those flows that show no such viscosity increases (Figures 1-3). This is reasonable, consistent with observations that lava flows tend to "pile up" as they cool. Both the linear and exponential viscosity models predict downstream widening and thickening. Since the model assumes volume conservation, such concomitant widening and thickening necessarily implies a decrease in flow rate.

Comparison of Data and Theory

By comparing the theoretical profiles predicted by the model with known flow dimensions, we can work "backward" to infer the rheology of geologic deposits. This can be a valuable method of studying lavas whose flow has not been recorded, including prehistoric flows and flows in remote areas on Earth or other planets. However, we note that this model is simplified and must be applied with caution. One key assumption is flow must be unconfined. Once a channel and/or levees have been formed, flow becomes confined and tends to maintain an equilibrium width. Furthermore, the underlying topography is assumed to be smooth and characterized by constant slope. It is essential that this condition be satisfied because a lava of constant viscosity flowing on irregular topography may form a deposit having dimensions similar to that of a lava flowing on a smooth surface that cools during flow. Finally, our model assumes downstream flow is driven by gravitational transport, as opposed to being driven by hydrostatic pressure. If these assumptions are satisfied by a given flow, matching the flow's geometric dimensions to those predicted by the model can be used to infer or constrain the governing rheology (i.e., the rheological parameters $\alpha=\alpha(x)$ and m). A quantitative comparison between such theoretical and actual profiles is the focus of this section. However, this comparison is restricted to width profiles: without a priori knowledge of preexisting topography, centerline depth profiles cannot be accurately constructed.

Data

The database for this analysis consists of eight basaltic lava flows (or segments thereof). Each flow included in this study is an individual flow unit, as compound flows or flow fields are not described by our model. In choosing suitable candidates for measurement, we used the following criteria: (1) unconfined, gravity-driven flow; (2) continuous, well-preserved and unobscured flow margin; (3) constant surface slope; and (4) relatively smooth substrate such that any irregularities in the substrate do not significantly affect flow behavior. Five of the eight lava flows analyzed are tholeiite basalts on Kilauea volcano that were observed directly in the field. These flows are individual pahoehoe toes, with lengths ranging from 0.6 to 5 m from the point of breakout. Three of these pahoehoe toes have ropy morphology; the remaining two are smooth-surfaced. We measured flow width as a function of distance from the source. For two ropy pahoehoe flows, we also constructed an additional longitudinal width profile: we measured the end-to-end widths of the ropes at various downstream locations. No such measurement could be made on the third ropy toe, as it had a double-rope morphology.

We also constructed longitudinal profiles of flow width of three basaltic lavas from remote sensing images: La Poruña (Andes, Chile), Marcath flow (Lunar Crater, United States) and SP flow (San Francisco Volcanic Field, United States); see Figure 4. Each of these lavas met the suitability criteria outlined above. These flows range in composition from alkali basalt to basaltic andesite and are several kilometers in length [*Schaber et al.*, 1980; *Lum et al.*, 1989, *Francis*, 1993].

Methodology

In this paper, we compare the model's theoretical profiles of flow width against measurements obtained from our field and photographic studies. To generate these profiles, the model requires a variety of input parameters. Some of these parameters (i.e., h_0 and θ) are easily measured; others (i.e., m and α) are unknown and must be deduced. Recall that m is characteristic of the fluid so its value remains constant during flow (e.g., Newtonian fluids have m=3), whereas the parameter α records changes in viscosity during flow. Our model assumes any cross-stream variations in α are negligible, that is, $\alpha=\alpha(x)$. We consider three end-member approximations for $\alpha(x)$, all based on the assumption that α is inversely related to viscosity. These three models for $\alpha(x)$, corresponding to constant, linearly increasing, and exponentially increasing viscosity, are given in (31). Note that our solution for flow depth (equation (28)) and half width (equation (29b)) is not sensitive to absolute values of α_0, only to the ratio of $\alpha_0/\alpha(x)$. Thus α_0 is a free parameter which we define as α_0=1. In all cases, we assume a point source (i.e., w_0=1).

Our approach is to first consider only the field data. These flows are sufficiently short (< 5 m) such that viscosity (and thus α) is assumed constant. Thus the only unknown input parameter is m, which can be deduced by a best fit of the model to the data. We assume this value of m to be characteristic of all basaltic lavas.

We then consider the remote sensing data. Over the length of these flows (2-8 km), significant cooling and/or crystallization may have occurred, resulting in a downstream

Figure 4a. Image of SP flow, located in the San Francisco Volcanic Field, United States. The flows in Figures 4a-4c are all basaltic and were selected according to the criteria described in the text.

Figure 4b. Image of Marcath flow, Lunar Crater, United States.

Figure 4c. Image of La Poruña flow, located in the Andes Mountains in northern Chile.

viscosity increase. Thus we cannot assume constant α. However, using the m value obtained from the field data above, the form of $\alpha(x)$ can be inferred for each flow by fitting the model to these data. By computing the corresponding predicted viscosity increase, the model can be tested for reasonableness.

Results: Field Data

In accordance with the above described methodology, we begin our analysis by comparing the field data with the theoretical output of our fluid dynamic model assuming constant viscosity. For the majority of the field data, the best fit of the model is obtained using m values of 1-2 (Figure 5). (We note, however, the data do not all appear concave as predicted by the constant-viscosity model.) We assume this value of m to be characteristic of all basaltic lavas.

As Newtonian fluids are characterized by $m=3$, our analysis suggests most basaltic flows are non-Newtonian.

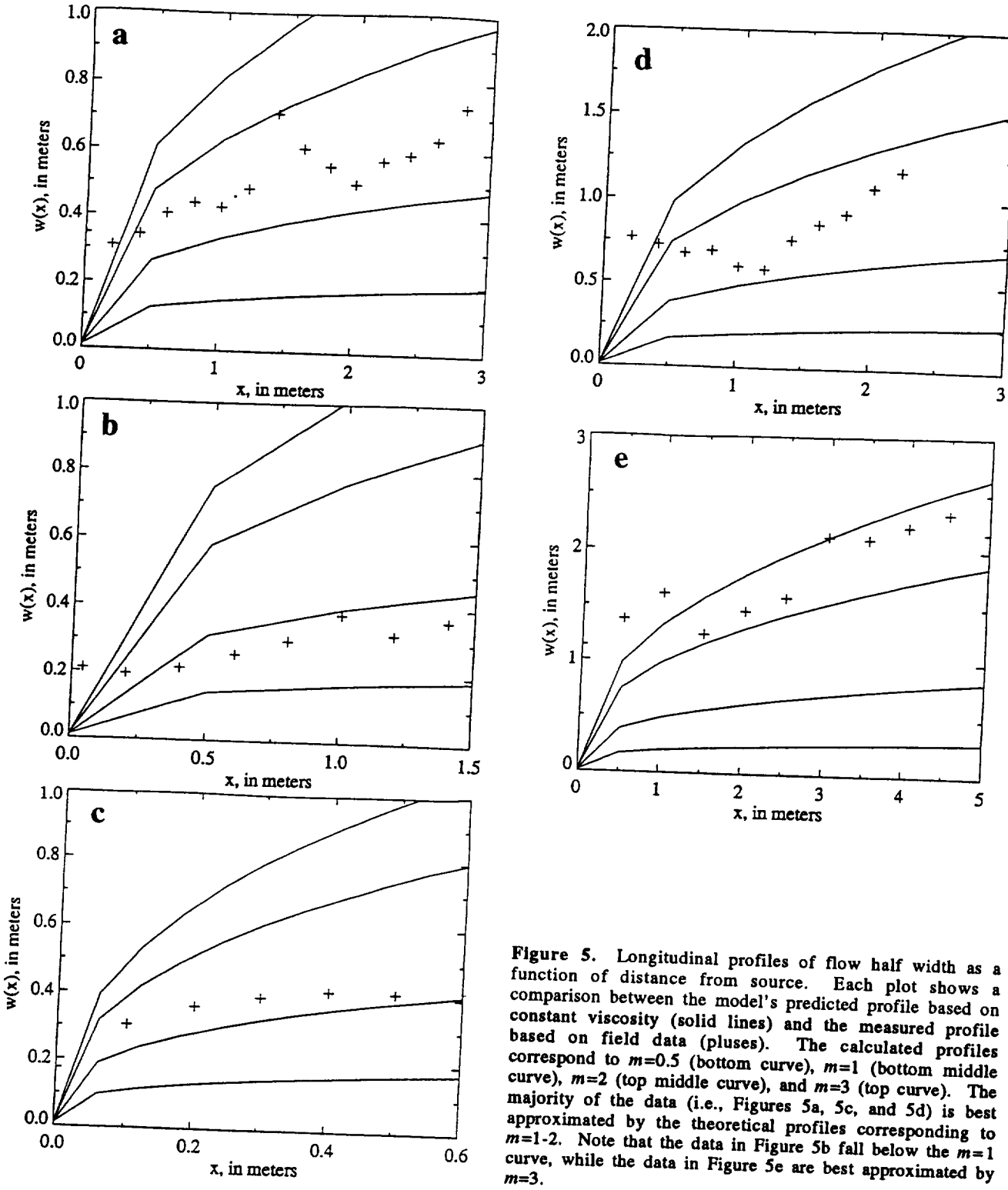

Figure 5. Longitudinal profiles of flow half width as a function of distance from source. Each plot shows a comparison between the model's predicted profile based on constant viscosity (solid lines) and the measured profile based on field data (pluses). The calculated profiles correspond to m=0.5 (bottom curve), m=1 (bottom middle curve), m=2 (top middle curve), and m=3 (top curve). The majority of the data (i.e., Figures 5a, 5c, and 5d) is best approximated by the theoretical profiles corresponding to m=1-2. Note that the data in Figure 5b fall below the m=1 curve, while the data in Figure 5e are best approximated by m=3.

Equation (4) predicts these basaltic flows, with their lower m values, to be thicker than Newtonian flows emplaced at the same flow rate. This is in agreement with a wide variety of field and laboratory measurements of basaltic lavas which indicate the presence of a yield strength [e.g., *Shaw et al.*, 1968; *Shaw*, 1969; *Pinkerton and Sparks*, 1978]. This non-Newtonian rheology has been attributed to dispersed crystals and gas bubbles contained in the lava and possibly to the development of molecular structural units at subliquidus temperatures (as summarized by *Cas and Wright* [1987, section 2.4]).

As discussed above, we also measured the widths of surface ropes as a function of downstream location of two pahoehoe flows. (Rope width is defined as the linear distance between the endpoints of each rope.) These data are shown along with the model's predicted longitudinal width profiles for various m (Figure 6). For both flows, the model approximates the data for $1/2 < m < 1$. Recall that our model assumes unconfined flow. We conducted these rope width measurements because we were interested in seeing how our model would fit data of confined flow. Like the flow itself, the ropes widen downstream. However, the downstream widening of the ropes is hampered by the confining effect of the previously established flow margins. Thus we might expect the ropes to experience less net widening compared to the total flow, corresponding to a smaller m value. This is precisely what Figure 6 shows.

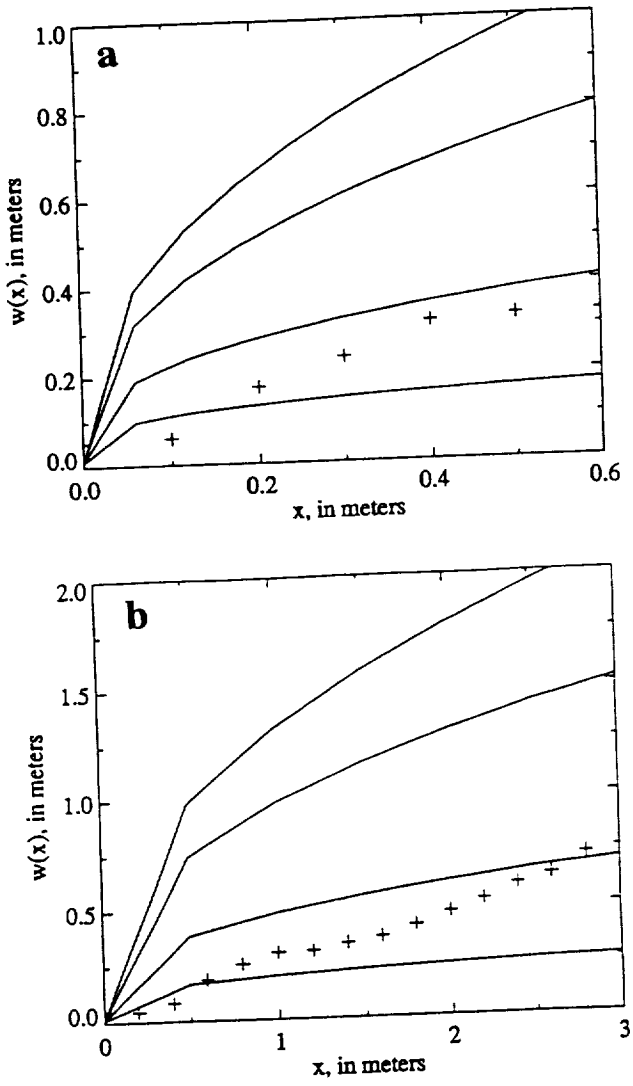

Figure 6. Longitudinal profiles of rope half width as a function of distance from source. Each plot shows a comparison between the model's predicted profile based on constant viscosity (solid lines) and the measured profile based on field data (pluses). The calculated profiles correspond to m=0.5 (bottom curve), m=1 (bottom middle curve), m=2 (top middle curve), and m=3 (top curve). These data are best approximated by the theoretical profiles corresponding to m=0.5-1.

Results: Remote Sensing Data

Using m values of 1 and 2, we run the model for parameters corresponding to the remote sensing data, based on the assumption of constant viscosity. Figure 7 shows the resulting longitudinal width profiles. For all flows, the data are inconsistent with the model's predictions. The measured widths generally exceed those predicted by the model, and these differences become more pronounced downstream. This results in a steeper longitudinal width profile than that predicted by the model. The inconsistency between these data and the model's predictions suggests that basaltic flows of these lengths are generally characterized by a downstream viscosity increase.

Using the same m values and initial parameters, we rerun the model based on the assumption of nonconstant viscosity. Figures 8 and 9 show longitudinal width profiles for linearly and exponentially increasing viscosities, based on (31b) and (31c), respectively. In these equations, the parameter L_α quantifies the downstream viscosity increase. In the absence of actual data or an empirical law, a value of L_α must be assumed. Choosing L_α sufficiently large has the effect of reducing (31b) and (31c) to (31a), the case of constant viscosity. In this work, our method is to first chose a value of L_α empirically to approximate the data and then to test this value for reasonableness by calculating the corresponding change in viscosity. This approach results in choices of L_α=50 (Figure 8) and L_α=500 (Figure 9).

Compared to the constant viscosity model, the linear viscosity model more closely approximates the data for all three flows (Figure 8). For two of these flows (Lunar Crater and SP), the exponential viscosity model also produces a good fit to the data (see Figures 9a and 9b). The downstream viscosity increases corresponding to the model predictions shown in Figures 8 and 9 are 2 and 3-4 orders of magnitude, respectively, over a distance of 4 km. These downstream viscosity increases are comparable to those documented for basaltic flows; see *Crisp et al.* [1994] for a review of the literature. The viscosity of the 1983-1984 Pu'u O'o flows has been measured by *Fink and Zimbelman* [1990] to have increased approximately 2 or 3 orders of magnitude during emplacement. *Moore and Ackerman* [1989] similarly estimate downstream viscosity increases of Kilauea basalts to be 2 orders of magnitude. For basaltic flows from Mount Etna, *Booth and Self* [1973] estimate viscosity increases of 2 orders of magnitude over 4 km. Thus the downstream viscosity increases corresponding to the linear and exponential viscosity profiles shown in Figures 8 and 9 are reasonable.

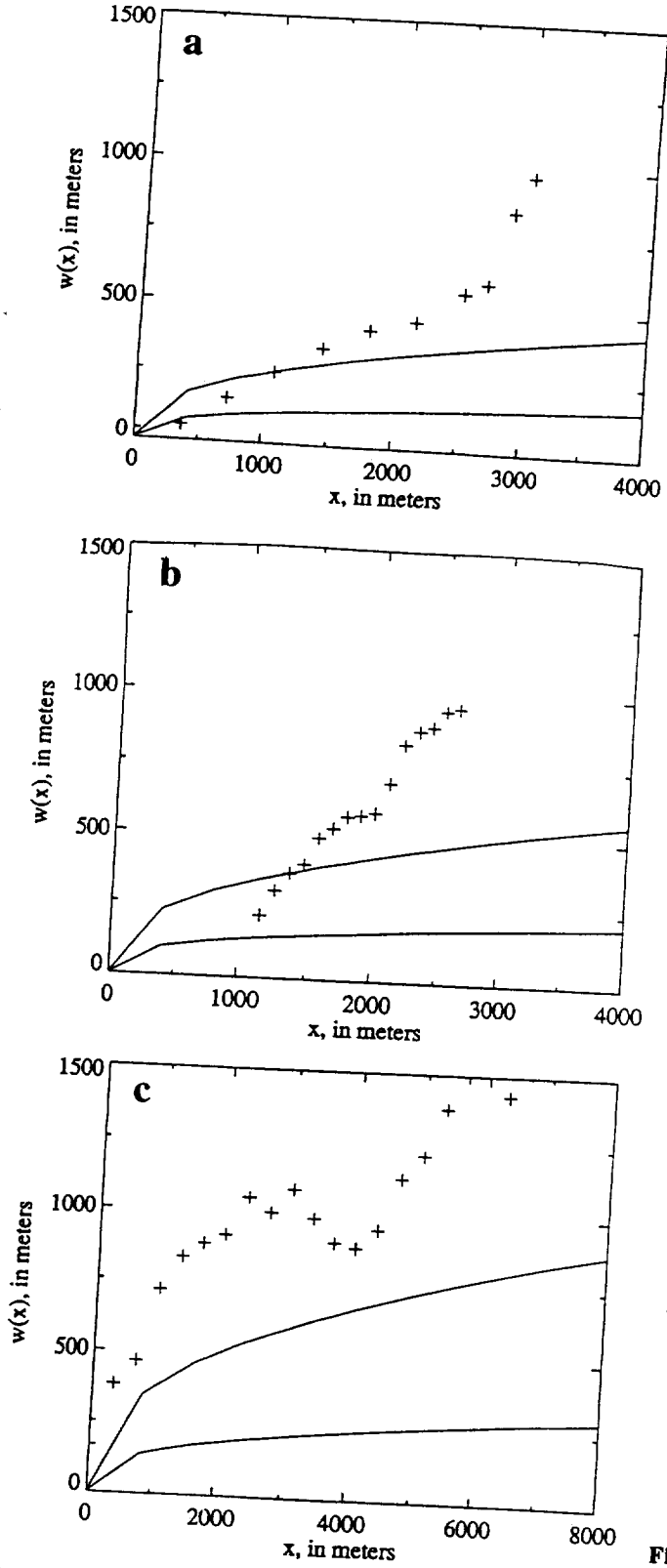

Figure 7. Longitudinal profiles of flow half width as a function of distance from source. Each plot shows a comparison between the model's predicted profile based on constant viscosity (solid lines) and the measured profile based on remote sensing data (pluses). The calculated profiles correspond to m=1 (bottom curve) and m=2 (top curve). Remote sensing data are of (a) SP flow, (b) Marcath Flow, Lunar Crater, and (c) La Poruña flow. In all cases, the data are steeper than the given theoretical profiles based on constant viscosity.

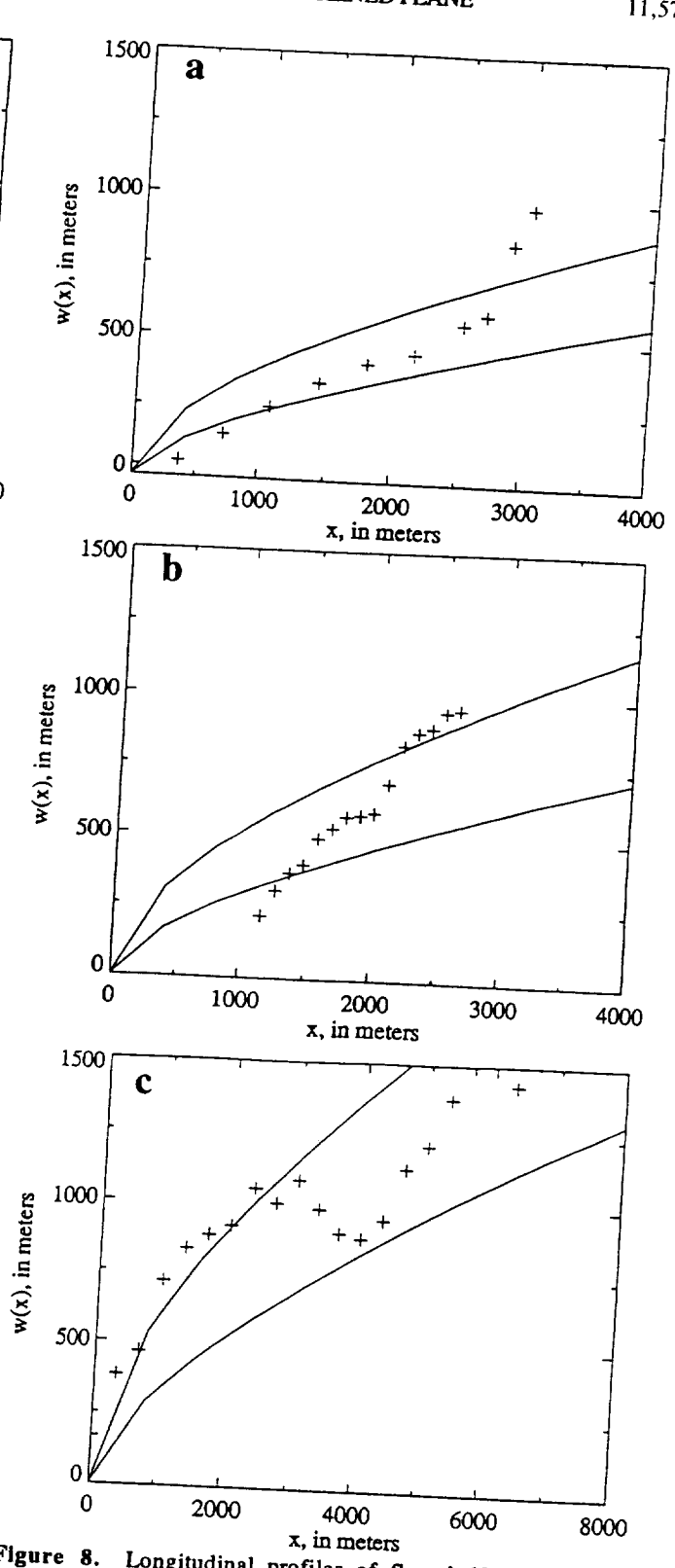

Figure 8. Longitudinal profiles of flow half width as a function of distance from source. Each plot shows a comparison between the model's predicted profile based on linear viscosity (solid lines) and the measured profile based on remote sensing data (pluses). The calculated profiles correspond to m=1 (bottom curve) and m=2 (top curve). For both profiles, L_α=50, which corresponds to a downstream viscosity increase of ~2 orders of magnitude over 4 km. Remote sensing data are of (a) SP flow, (b) Marcath Flow, Lunar Crater, and (c) La Poruña flow. Data of all three flows are better approximated by this linear viscosity model than the constant viscosity model shown in Figure 7.

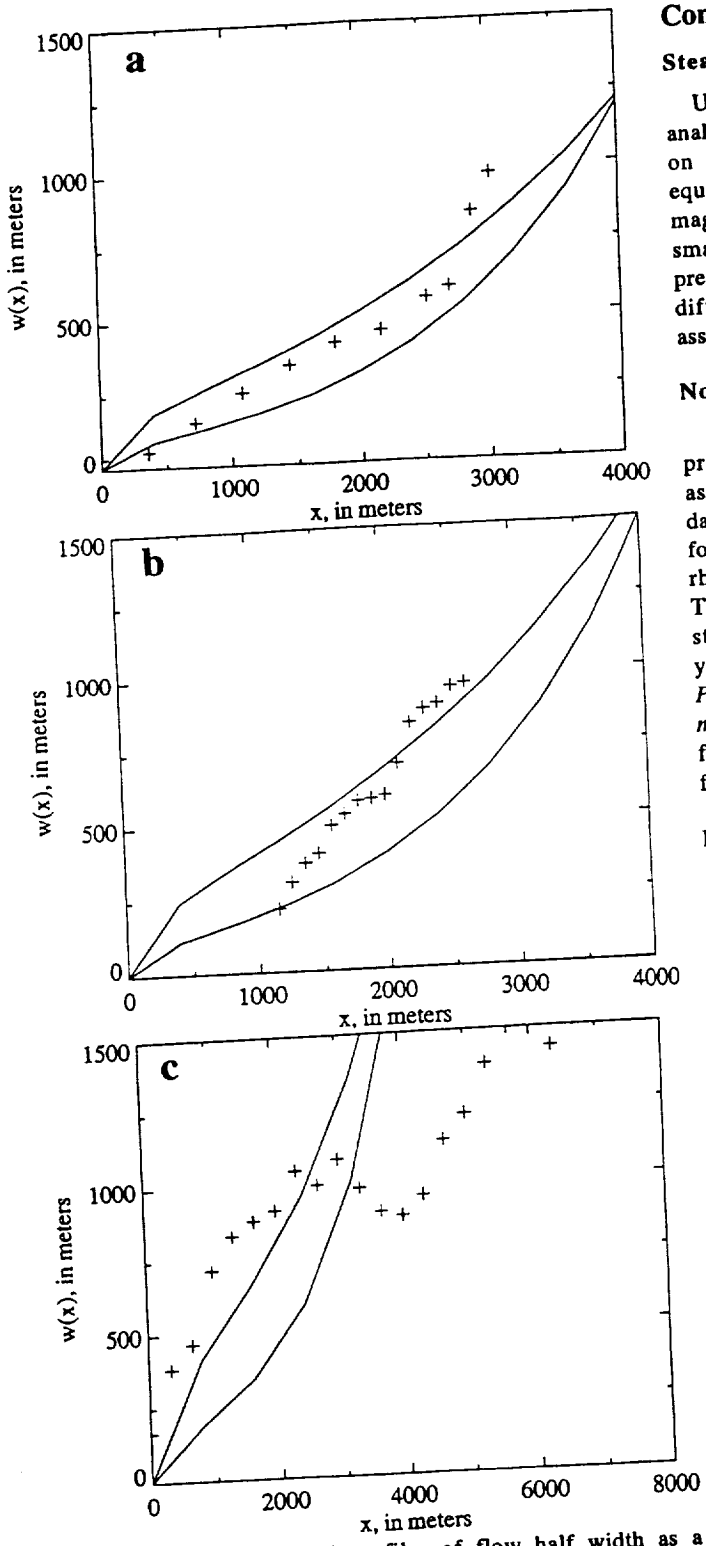

Figure 9. Longitudinal profiles of flow half width as a function of distance from source. Each plot shows a comparison between the model's predicted profile based on exponential viscosity (solid lines) and the measured profile based on remote sensing data (pluses). The calculated profiles correspond to m=1 (bottom curve) and m=2 (top curve). For both profiles, L_α=500, which corresponds to a downstream viscosity increase of 3-4 orders of magnitude over 4 km. Remote sensing data are of (a) SP flow, (b) Marcath Flow, Lunar Crater, and (c) La Poruña flow. The data in Figures 9a and 9b are better approximated by this exponential viscosity model than the constant viscosity model shown in Figure 7.

Conclusions

Steady State Similarity Solution

Using a similarity transformation, we found an exact analytic solution in the steady state for gravity-driven flows on an inclined plane. In formulating the governing equation, we assumed that volume is conserved and that the magmastatic pressure gradient in the downstream direction is small relative to the influence of gravity. Our solution predicts downstream changes in flow depth and width for different rheological characteristics based on known or assumed initial parameters.

Non-Newtonian Rheology

Figure 5 shows a comparison of longitudinal width profiles of sample field data and model predictions, assuming constant viscosity. The majority of these field data are well approximated by the constant viscosity model, for m between 1 and 2. This indicates non-Newtonian rheology, as Newtonian fluids are characterized by m=3. This is in agreement with numerous field and laboratory studies of basaltic lavas which indicate the presence of a yield strength [e.g., *Shaw et al.*, 1968; *Shaw*, 1969; *Pinkerton and Sparks*, 1978]. Physically, the relatively low m values of these basaltic flows indicate relatively thin flows, compared with Newtonian flows emplaced at the same flow rate.

Downstream Viscosity Increases

Using m values of 1 and 2, we ran the model for three end-member approximations of α: corresponding to constant, linearly increasing and exponentially increasing viscosity. The remote sensing data are inconsistent with the model's predictions for constant viscosity (constant α). Instead, they are better approximated by linear or exponential models corresponding to downstream viscosity increases of 2-4 orders of magnitude, over a distance of 4 km. The reasonableness of these values attests to the validity of this model.

Notation

q	volumetric flow rate per unit width.
x	spatial coordinate in the downstream direction (parallel to slope).
y	spatial coordinate in the cross-stream direction (perpendicular to slope).
z	spatial coordinate related to x, defined in equation (13).
t	time.
α	a spatially dependent, empirically determined rheological parameter.
α_0	α at the source.
h	flow depth.
h_0	flow depth at the source.
w	flow half width.
w_0	flow half width at the source.
b	an empirically determined constant.
m	an empirically determined positive constant.
g	gravitational acceleration.
ν	kinematic viscosity.
θ	slope.
$f(\theta)$	some function of slope.

L	characteristic length scale.
L_α	scaling factor for α.
a, r, q	constants of similarity construct, defined in terms of m in equation (26).
ξ, G, η	variables of similarity construct, defined in equations (15) and (16).

Acknowledgments. This research was funded by NASA grants NGT 50930 and NAGW 3684. We thank L. Glaze, D.F. McTigue, G. Weir and an anonymous reviewer for their thoughtful reviews. This manuscript also benefited from useful discussions with D. Bercovici and X. Tata (University of Hawaii) and S. Blake (The Open University). Images were provided by R. Lopes-Gautier (Jet Propulsion Laboratory, NASA) and P. Francis (The Open University). Many thanks to University of Hawaii staff M. Tatsumura (field assistance) and H. Garbeil (computer programming). This is SOEST contribution 4068 and HIGP paper 875.

References

Baloga, S., Lava flows as kinematic waves, *J. Geophys. Res.*, *92*, 9271-9279, 1987.

Booth, B., and S. Self, Rheological features of the 1971 Mount Etna lavas, *Philos. Trans. R. Soc. London A*, *274*, 99-106, 1973.

Bruno, B.C., G.J. Taylor, S.K. Rowland, P.G. Lucey, and S. Self, Lava flows are fractals, *Geophys. Res. Lett.*, *19*, 305-308, 1992.

Bruno, B.C., G.J. Taylor, S.K. Rowland, and S.M. Baloga, Quantifying the effect of rheology on lava-flow margins using fractal geometry, *Bull Volcanol.*, *56*, 193-206, 1994.

Cas, R.A.F., and J.V. Wright, *Volcanic Successions*, 528 pp., Allen and Unwin, Winchester, Mass., 1987.

Crisp, J., K.V. Cashman, J.A. Bonini, S.B. Hougen, and D.C. Pieri, Crystallization history of the 1984 Mauna Loa lava flow, *J. Geophys. Res.*, *99*, 7177-7198, 1994.

Fink, J.H., and J. Zimbelman, Longitudinal variations in rheological properties of lavas: Puu Oo basalt flows, Kilauea Volcano, Hawaii, in *Lava Flows and Domes. Emplacement Mechanisms and Hazard Implications*, edited by J.H. Fink, pp. 157-173, Springer-Verlag, New York, 1990.

Francis, P., *Volcanoes*, 443 pp., Oxford Univ. Press, New York, 1993.

Gol'din, B.M., and L.S. Lyubashevskiy, Computation of the velocity of mudflows in Crimean rivers, *Tr. Ukr. Nauchno Issled. Gidrometerol. Inst.*, *60*, 73-75, 1966.

Hunt, B., Asymptotic solution for dam-break problem, *J. Hydraul. Div. Am. Soc. Civ. Eng.*, *108*, 115-127, 1982.

Huppert, H.E., The propagation of two-dimensional and axisymmetric viscous gravity currents over a rigid horizontal surface, *J. Fluid Mech.*, *121*, 43-58, 1982a.

Huppert, H.E., Flow and instability of a viscous current down a slope, *Nature*, *300*, 427-429, 1982b.

Lighthill, M.J., and G.B. Whitham, On kinematic waves, I, Flood movement in long rivers, *Proc. R. Soc. London A*, *229*, 281-316, 1955.

Lister, J.R., Viscous flows down an inclined plane from point and line sources, *J. Fluid Mech.*, *242*, 631-653, 1992.

Lum, C.C.L., W.P. Leeman, K.A. Foland, J.A. Kargel, and J.G. Fitton, Isotopic variations in continental basaltic lavas as indicators of mantle heterogeneity: Examples from the western U.S. Cordillera, *J. Geophys. Res.*, *94*, 7871-7884, 1989.

Moore, H.J., and J.A. Ackerman, Martian and terrestrial lava flows (abstract), *Lunar Planet. Sci., XX*, 711-712, 1989.

Nye, J.F., The response of glaciers and ice sheets to seasonal and climatic changes, *Proc. R. Soc. London A*, *256*, 559-584, 1960.

Nye, J.F., The response of a glacier to changes in the rate of nourishment and wastage, *Proc. R. Soc. London A*, *275*, 87-112, 1963.

Paterson, W.S.B., *The Physics of Glaciers*, 250 pp., Pergamon, Tarrytown, N.Y., 1969.

Pinkerton, H., and R.S.J. Sparks, Field measurements of the rheology of lava, *Nature*, *276*, 383-386, 1978.

Schaber, G.G., C. Elachi and T.G. Farr, Remote sensing data of SP mountain and SP lava flow in North-central Arizona, *Remote Sensing Environ.*, *9*, 149-170, 1980.

Shaw, H.R., Rheology of basalt in the melting range, *J. Petrol.*, *10*, 510-535, 1969.

Shaw, H.R., T.L. Wright, D.L. Peck and A.R. Okamura, The viscosity of basaltic magma: An analysis of field measurements in Makaopuhi lava lake, Hawaii, *Am. J. Sci.*, *266*, 225-264, 1968.

Sherman, B., Kinematic wave models for overland flow, *Appl. Math.*, *35*, 435-444, 1978.

Sherman, B., Channel flow with infiltration, *Appl. Math.*, *39*, 87-96, 1981.

Sherman, B., and V.P. Singh, A kinematic model for surface irrigation, *Water Resour. Res.*, *14*, 357-364, 1978.

Smith, P., A similarity solution for slow viscous flow down an inclined plane, *J. Fluid Mech.*, *58*, 275-288, 1973.

Weir, G.J., Kinematic wave theory for Ruapehu lahars, *N. Z. J. Sci.*, *25*, 197-203, 1982.

Weir, G.J., The asymptotic behaviour of simple kinematic waves of finite volume, *Proc. R. Soc. London A*, *387*, 459-467, 1983.

S. M. Baloga, Proxemy Research Inc., 20528 Farcroft Lane, Laytonsville, MD 20882.

B. C. Bruno, Department of Earth Sciences, The Open University, Walton Hall, Milton Keynes MK7 6AA, England. (e-mail: B.C.Bruno@open.ac.uk)

G. J. Taylor, Hawaii Institute of Geophysics and Planetology, University of Hawaii at Manoa, 2525 Correa Road, Honolulu, HI 96822. (e-mail: gjtaylor@kahana.pgd.hawaii.edu)

(Received August 10, 1995; revised December 21, 1995; accepted January 5, 1996.)